Correlating quasiparticle excitations with quantum femtosecond magnetism in photoexcited nonequilibrium states of insulating antiferromagnetic manganites

P. C. Lingos, A. Patz, T. Li, G. D. Barmparis, A. Keliri, M. D. Kapetanakis, L. Li, J. Yan, J. Wang, and I. E. Perakis

Phys. Rev. B **95**, 224432 — Published 28 June 2017

DOI: 10.1103/PhysRevB.95.224432

Correlating Quasi–Particle Excitations with Quantum Femtosecond Magnetism in Photoexcited Non–Equilibrium States of Insulating Anti–Ferromagnetic Manganites

P. C. Lingos,[1] A. Patz,[2] T. Li,[2] G. D. Barmparis,[1] A. Keliri,[3] M. D. Kapetanakis,[4] L. Li,[5] J. Yan,[5] J. Wang,[2] and I. E. Perakis[4,1]

[1]*Department of Physics and Crete Center for Quantum Complexity and Nanotechnology, University of Crete, Box 2208, Heraklion, Crete, 71003, Greece*

[2]*Ames Laboratory and Department of Physics and Astronomy, Iowa State University, Ames, Iowa 50011, U.S.A.*

[3]*Department of Physics, University of Crete, Box 2208, Heraklion, Crete, 71003, Greece*

[4]*Department of Physics, University of Alabama at Birmingham, Birmingham, Alabama 35294, U.S.A*

[5]*Department of Materials Science and Engineering, University of Tennessee, Knoxville, Tennessee 37996, U.S.A*

(Dated: June 6, 2017)

We describe a mechanism for insulator–to–metal transition triggered by spin–canting following fs laser–excitation of insulating anti–ferromagnetic (AFM) states of colossal magneto-resistive (CMR) manganites. We show that photoexcitation of composite fermion quasi–particles dressed by spin fluctuations results in the population of a broad metallic conduction band due to canting of the AFM background spins via strong electron–spin local correlation. By inducing spin–canting, photoexcitation can increase the quasi–particle energy dispersion and quench the charge excitation energy gap. This increases the critical Jahn–Teller (JT) lattice displacement required to maintain an insulating state. We present fs–resolved pump–probe measurements showing bi–exponential relaxation of the differential reflectivity below the AFM transition temperature. We observe a nonlinear dependence of the ratio of the *fs* and *ps* relaxation component amplitudes at the same pump fluence threshold where we observe femtosecond magnetization photoexcitation. We attribute this correlation between nonlinear fs spin and charge dynamics to spin/charge/lattice coupling and population inversion between the polaronic majority carriers and metallic quasi–electron minority carriers as the lattice displacement becomes smaller than the critical value required to maintain an insulating state following laser–induced spin canting.

PACS numbers: 78.67.Wj, 73.22.Pr, 78.47.J-,78.45.+h

INTRODUCTION

The spin– and charge–ordered phases of quantum materials are traditionally switched by tuning static parameters such as chemical dopants, pressure, or magnetic fields. Spontaneous coherence induced in this way, e.g. between many–body states separated by the Mott–Hubbard insulator gap, can establish new ordered phases via equilibrium phase transitions. The question then arises whether non–equilibrium phase transitions can be similarly triggered by laser–induced charge fluctuations [1, 2] and non–thermal populations of many–body states [3]. In this way, femtosecond (fs) laser pulses can be used to create a quasi–instantaneous electronic "initial condition" for non–adiabatic time evolution prior to lattice thermalization [4–8]. The physical properties of complex materials such as the manganites [9] are governed by collective order and fluctuations of coupled degrees of freedom [10–14]. This results in elementary excitations and order parameters with coupled charge, orbital, spin, and lattice components, which makes it difficult to underpin their microscopic composition [8, 15–19]. In the manganites, while strong coupling of electronic, magnetic, and lattice degrees of freedom is believed to be responsible for the emergence of coexisting insulating/lattice–distorted/AFM and metallic/undistorted/FM nanoscale regions [9], the relevant quasi–particles have not been fully characterized yet [19]. Some theoretical studies have proposed that the sensitivity to the non–thermal electronic perturbations leading to the CMR phase transition from AFM/insulating to FM/metallic state may be due to delocalized electrons with mobility mediated by classical spin–canting [15, 20, 21], which coexist with the polaronic carriers that dominate in the insulating ground state [22–24].

In quantum materials, two different pathways may lead to a photo-induced phase transition [25]: (1) electronic pathway, triggered by photo–excitation and subsequent relaxation of electronic and spin populations can also change the lattice potential in the excited state, (2) lattice pathway, which may lead to a delayed crystallographic phase transition that typically completes within ps timescales [26]. Here we are mostly interested in the first stage of the time–dependent process, which is initiated by fs laser excitation of AFM insulating systems such as the manganites. In VO_2 [25] and $TiSe_2$ [8] systems, experiments have shown that a highly non-equilibrium initial condition is set by quasi-instantaneous electronic processes induced by the photo–carriers, which can lead to metastable states prior to an insulator–to–metal phase transition [8, 27]. For example, in the $TiSe_2$ insulator, the electronic component of the charge density wave order parameter is quenched quasi-instantaneously while the lattice component persists [8]. This results in a non–equilibrium state with lattice order similar to equilibrium, whose properties are controlled by the photoinduced change in the local electronic density matrix [8]. In VO_2, a metastable metallic phase with the monoclinic lattice structure of the insulating phase is observed after the electronic component has switched from insulating to metallic [27]. Here we investigate the possible role in a non–equilibrium phase transition of spin fluctuations driven by photo–carrier populations interacting with a deformable spin and lattice medium.

In low-bandwidth insulating manganites such as the $Pr_{0.7}Ca_{0.3}MnO_3$ system (PCMO) studied experimentally here, metallic phases cannot be accessed by tuning the temperature [9]. An AFM insulator to FM metal equilibrium phase transition can, however, be induced non–thermally, e.g. by applying a strong magnetic field, which leads to CMR. While in equilibrium a magnetic field simultaneously changes the coupled electronic, magnetic, and lattice order components, several ultrafast spectroscopy experiments [13, 14, 28–36] have observed non–thermal fs charge and/or spin dynamics prior to electron–lattice relaxation. While a new lattice structure seems to be established after ps timescales, electronic, orbital, and magnetic orders have been observed to change much faster. Photo-induced non-equilibrium phase transitions are typically characterized by a nonlinear threshold dependence of the measured properties on the pump laser fluence. The time evolution of the charge, orbital, lattice, and magnetic components of a complex order parameter can be separately monitored with fs X-ray diffraction (XRD) [28, 29]. The fs dynamics of AFM order is less understood, as it may involve an AFM→FM transition initiated by charge excitations. Ref. 4 reported a threshold increase of the fs-resolved magneto-optical Kerr (MOKE) and circular dichroism (MCD) signals at 100fs time delays, which is absent at ps time delays and only appears below the AFM transition (Neel) temperature when a small magnetic field breaks the symmetry. This fs nonlinearity was interpreted in terms of an AFM→FM transition that occurs prior to the ps spin–lattice relaxation [4]. It was proposed that *quantum femtosecond magnetism* [6] and FM correlation may arise from both laser–driven charge fluctuations and non-thermal electronic populations. However, the microscopic link between spin and charge excitations in the fs temporal regime requires further clarification.

Few ultrafast spectroscopy experiments suggest a link between fs spin and charge laser–induced dynamics of an AFM–ordered insulating phase. The magneto-optical Kerr measurements by Miyasaka et.al. [30] show that ultrafast excitation of the charge degrees of freedom of the $Nd_{0.5}Sr_{0.5}MnO_3$ CE–type AFM ground state leads to a *ps* AFM→FM transition. The initial increase of the magnetic moment within 1ps was attributed to non–thermal spin–flip electronic scattering in the excited state. This is followed by a much slower magnetization increase due to spin–lattice thermalization, which slows down close to the AFM transition temperature. Matsubara et.al. [31] argued that a *ps* phase transition develops in several steps following fs photoexcitation of the $Gd_{0.55}Sr_{0.45}MnO_3$ AFM/CO/OO ground state. First, a metallic state develops after 100fs and decays within 1ps, while the magnetization grows within 500fs and decays within 10ps. The fast magnetization component increases with pump intensity, indicating that it arises from a microscopic mechanism that involves the excited photo-electrons. Okimoto et al [32] observed that 100fs photoexcitation of $Gd_{0.55}Sr_{0.45}MnO_3$ leads to metallic behavior of the conductivity within 200fs. The insulator gap decreases within 100fs timescales, well before lattice thermalization, and triggers the subsequent dynamics. The differential reflectivity displayed two relaxation components, fast ($\sim$280fs) and slow (1ps). For low intensity, the ps component was smaller than the fs component and increased linearly with pump power, while the fast fs component dominated for high intensity. Wall et. al. [33] studied the A-type AFM insulating state of $LaMnO_3$, where the spins align in FM planes that are AFM-coupled along the perpendicular c-axis. They found that the amplitude and damping of coherent lattice vibrations exhibit a sharp discontinuity at the Neel temperature, unlike for the background signal that showed smooth dependence on temperature. The observation of a $\sim$50-100fs relaxation component of the differential reflectivity indicates that an ultrafast spin–correlation mechanism is at work in the photoexcited state during non-thermal timescales, where electronic processes and the tunneling between the AFM–coupled FM planes can play an important role.

Pulsed X–ray measurements of the individual order parameter components can distinguish electronic, lattice, and spin signals. Forst et al [29] measured the time evolution of the magnetic and orbital order of the LaSrMnO manganite and compared the results between mid-infrared (tuned at 92meV) and near-infrared (tuned at 1.5eV) pump photoexcitation. While the near–infrared photoexcitation of the electronic degrees of freedom changes the AFM order on a fast 250fs timescale, the mid–infrared excitation of lattice degrees of freedom leads to much slower ($\sim$ 10ps) dynamics. This experimental result indicates that fs changes in the magnetic properties triggered by spin–photoelectron coupling should be distinguished from the slower spin–lattice relaxation. Ehrke et. al. [34] studied the $La_{0.5}Sr_{1.5}MnO_4$ AFM state with ultrafast XRD and showed that, while fs photoexcitation melts the AFM spin order, the orbital order is only partly reduced. This observation was attributed to a metastable FM state induced by the charge redistribution between different lattice sites following fs laser excitation. Unlike in the conventional double–exchange mechanism [37], the charge excitations were found to change the short–range magnetic correlations and cant the AFM spins prior to melting of the JT-distorted lattice. Beaud et.al. [28] used time-resolved XRD to show that the dynamics of the phase transformation may be described phenomenologically by a single time-dependent parameter determined by the photo–carrier populations. They proposed that a phenomenological potential with time–dependent spring constant can describe the dynamics based on classical equations of motion for three coupled lattice modes. Matsuzaki et.al. [35] studied the ultrafast dynamics of charge and orbital order melting in $Nd_{0.5}Ca_{0.5}MnO_3$ by using 20fs pulses with low intensity and concluded that, although charge order melts within 30fs via strong electronic correlations, the oxygen displacements associated with the orbitally–ordered ordered phase persist and are only released later. Polli et.al. [13] found that melting of the charge order in PCMO occurs non-instantaneously within 50fs, later than in $Nd_{0.5}Ca_{0.5}MnO_3$. This delayed charge response was attributed to cooperative and nonlinear effects for high pump intensities. Finally, Singla et. al. [36] reported a 18fs bottleneck for the loss of orbital order following photo-

excitation of $La_{0.5}Sr_{1.5}MnO_4$ with 4fs laser pulses. The observation of a threshold in the fluence dependence of the JT phonon amplitude is consistent with a cooperative response for high photo-carrier density.

To interpret ultrafast spectroscopy experiments such as the above, a quantum theory of coupled spin and charge dynamics in systems with deformable spin and lattice backgrounds is needed. Model Hamiltonians studied with different theoretical techniques must be used to make progress in understanding strongly correlated systems [38]. In this paper we propose a possible mechanism for photoinduced insulator to metal transition triggered by transient spin–canting that changes the excited quasi–particle energy dispersions, which is based on the interplay between a quasi–instantaneous electronic/magnetic pathway and a delayed lattice pathway. We discuss the possible role of "soft" composite fermion quasi–particle energy bands that are modified by fs laser excitation and strong electron–magnon quantum fluctuations. We note that the latter have been observed to significantly change the spin–wave energy dispersion and lifetimes in metallic manganites [39–41]. Our calculations are based on a generalized tight–binding model taken from the manganite literature [9, 19]. We treat the local Mn + O multi–electron configurations and strong magnetic exchange correlations by introducing Hubbard composite fermion operators [17, 42]. We present numerical results for a CE–type AFM/CO/OO unit cell showing strong coupling of the AFM chains and planes that characterize the insulating states of the manganites [9, 19, 21]. due to quantum spin fluctuations coupled to the charge excitations. In particular, such strong electron–magnon coupling delocalizes the excited quasi–particles due to the deformation of the AFM spin background during the electronic hopping. We show that the non–perturbative dependence of the quasi–particle energy disperions on local spin canting leads to a broad metallic conduction band and quenching of the insulator energy gap. As a result, the critical value of the Jahn–Teller (JT) lattice displacement necessary for stabilizing an insulating state increases, which can lead to an ultrafast transition to a metallic state following photoexcitation of FM correlation.

The experimental observation of threshold nonlinear dependence of pump–probe signals on the pump fluence is typically associated with photoinduced phase transitions. Here we present experimental results showing a threshold non–linear pump–fluence dependence of both fs differential reflectivity and fs magneto–optical signals below the transition to AFM order. In particular, the ratio of the amplitudes of the "fast" (fs) and "slow" (ps) relaxation components of a two–step bi–exponential relaxation of the differential reflectivity signal below the Neel temperature grows nonlinearly with pump–fluence close to the threshold for *fs* AFM→FM switching observed in both Kerr effect (MOKE) and magnetic circular dichroism (MCD) signals at ∼100fs. We propose that a possible interpretation of the above experimental nonlinearities involves an inverted photoexcited state above a pump fluence threshold, where fast, mobile, metallic quasi–electrons dressed by quantum spin fluctuations coexist with the polaronic carriers that populate the ground state. Laser excitation then results in ultrafast charge redistribution between JT–distorted and undistorted sites, which changes the energy gap, spin properties, and lattice distortions.

The paper is organized as follows. In Section II we outline our theoretical model and discuss its relevance to the manganites. In Section III we discuss the photoexcitation of spin dynamics and present a quantum kinetic calculation of non–adiabatic FM short–range correlation arising from quantum spin fluctuations. In Section IV we present our quantum kinetic theoretical formulation of the charge–spin coupled dynamics of composite fermion quasi–particles. In Section V we calculate the itinerant quasi-particle energy dispersions within a Hubbard–I mean–field approximation and compare with bare electrons and holes moving in an adiabatically–decoupled classical spin background. In Section VI we propose a theoretical picture of a fs photoinduced insulator to metal transition driven by spin dynamics. In Section VII we present fs–resolved pump–probe experimental results showing the emergence of two different (*fs* and *ps*) relaxation components below the AFM transition temperature, whose amplitude ratio displays a nonlinear dependence at the pump fluence threshold necessary for fs magnetization photogeneration. In Section VIII we discuss our conclusions and implications of our results and, lastly, we summarize the theoretical calculations in the appendix.

THE MODEL AND ITS RELATION TO THE MANGANITES

Our generalized tight–binding model is based on Hubbard operators that describe charge excitations bertween the local multi–electron configurations [17]. We assume that the charge at each site i fluctuates between multi–electron configurations $|i\alpha M\rangle$, with total spin (J,M), and $|im\rangle$, with total spin (S,m). The above electronic configurations are assumed to be eigenstates of the local Hamiltonian [17] that describes all on–site interactions, including the strong electron–lattice and magnetic exchange (Hund's rule) interactions. In the manganites, these correspond to Mn + O hybridized states analogous to the Zhang–Rice local singlet between the O hole and the Cu^{2+} ion in the Cu–oxide superconductors [43], which can justify the use of a generalized tight-binding model [19] and is consistent with the ab–initio results of Ref. 44.

The motion of an itinerant spin–1/2 electron is restricted by its strong magnetic exchange interaction J_H with the localized spins on each site [37] and by the energy barrier E_{JT} between JT–distorted and undistorted site local configurations. J_H originates from Hund's rule and typically exceeds the kinetic energy bandwidth (strong coupling limit) [9, 21]. We describe such strong local FM correlation between the itinerant and localized electron spins by introducing magnetic Hubbard bands [17, 42] characterized by the total spin quantum numbers (J, M) and note that the population of $J = S-1/2$ states is suppressed. The local electron–lattice interaction is charac-

terized by two different parameters: (i) ratio of the JT energy barrier E_{JT} over the electron hopping energy t, (ii) adiabaticity parameter, given by the ratio of phonon energy $\hbar\omega_{ph}$ over t [21]. In the manganites, the JT phonon energy ($\sim$70meV) is smaller that the electron hopping energy (t $\sim$200meV) [9], which implies that hopping between sites is faster than the lattice rearrangements that accompany it [21]. Similar to previous works [9, 45, 46], we can then assume that the electronic energy levels depend on classical lattice coordinates.

In our calculations, the AFM order was modelled with a CE–AFM unit cell. Such insulating ground state with charge order (CO) and orbital order (OO) is observed, e.g., in the PCMO manganite studied experimentally here and in several half–doped manganites. The unit cell, Fig. 1(a), consists of inequivalent alternating "bridge" and "corner" lattice sites populated by Mn + O octahedra with different charge, spin, and JT distortions as observed experimentally [47]. These Mn + O clusters order along charge–modulated zig–zag chains with FM spins [9, 44]. Different chains are AFM–coupled and stacked in AFM–coupled planes (Fig. 1(a)). The JT distortions stabilize OO by splitting the degenerate states at the bridge sites, which enhances the population of the Mn 3d orbitals pointing along the zig–zag chain [9, 44]. As several experiments report that the Mn valence is similar between bridge and corner sites, the charge modulation most likely involves the total charge of the Mn + O local clusters, rather than Mn^{3+}/Mn^{4+} ions as originally thought [9]. For example, the calculations of Ferrari et. al. [44] suggest that, in the less distorted corner sites of the zig–zag FM chain, the role of the Mn^{4+} core spin is played by a Mn atom strongly hybridized with spin–polarized oxygen holes. On the other hand, the bridge sites are populated by a Mn^{3+} ion surrounded by a JT–distorted oxygen octahedron. In our model, we describe the Mn + O corner states in terms of "core spin" states $|im\rangle$, $m = -S, \cdots, S$, with S $\approx$3/2 [44]. In the bridge sites, we consider an electronic configuration $|i\alpha M\rangle$, $M = -J \cdots J$, with total spin $J = S + 1/2 \approx 2$, whose energy is lower by E_{JT} as compared to the corner site configurations due to the JT lattice distortion.

The main purpose of this paper is to discuss the possible role of spin fluctuations in laser–induced insulator→metal and AFM→FM non–equilibrium phase transitions. Within classical spin scenarios, the itinerant electrons move on top of an adiabatically–decoupled spin background with their spins FM–locked to the localized electron spins at each site: M=S+1/2 and m=S. Such an adiabatic picture assumes that the electronic hopping fluctuations occur on a time scale faster than the spin dynamics, so the spins always point along the spin–canting classical angles θ_i. For AFM–coupled chains as in the CE–AFM state Fig. 1(a), spin conservation then restricts the electronic motion inside a single FM chain for large J_H, due to the magnetic exchange energy cost for creating an anti–parallel spin configuration [9]. On the other hand, quantum spin fluctuations allow the electrons to hop on sites with anti–parallel spins by flipping the localized spins via $J_H S_i^{\pm} \cdot s_i^{\mp}$. The electrons can then form states with J =S+1/2

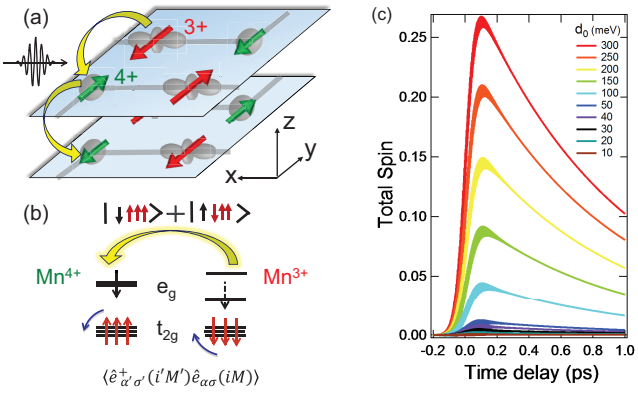

FIG. 1. (Color online) (a) Illustration of the inter–site electronic excitations in the CE–AFM/CO/OO three–dimensional unit cell considered here, which consists of 16 sites in two stacked AFM planes and two AFM–coupled FM zig–zag chains with alternating JT–distorted (bridge) and undistorted (corner) sites [9]. (b) Hopping of a composite fermion quasi–particle between two AFM sites induces quantum spin canting by forming a local state with total spin M=$S-1/2$ and J = S+1/2. Such inter–site charge–spin coupling is described by the Hubbard oparator amplitudes $\langle \hat{e}^{\dagger}_{\alpha'\sigma'}(i'M')\hat{e}_{\alpha\sigma}(iM)\rangle$ as discussed in the text. (c) Calculated time–dependence of the total z–component S_z(t) of the two AFM core spins discussed in the text, driven by the coupling of a 100fs optical field pulse, for population lifetime T_1=1ps and different Rabi energies d_0.

but $M = S - 1/2$ or smaller via electron–magnon quantum fluctuations [39–41].

The motion of an itinerant electron is restricted by spin–exchange, electron–lattice, and Mn + O local correlations. To take this into account, we project the electron operator in terms of composite fermion excitations with total charge e, which are created by the Hubbard operators [17, 42]

$$\hat{e}^{\dagger}_{\alpha\sigma}(iM) = |i\alpha M\rangle\langle i, M - \frac{\sigma}{2}|, \qquad (1)$$

on each site i, where σ=$\pm$ 1 labels the z–component of the local excitation total spin ($\hbar$ =1). These Hubbard operators obey the non–canonical anti–commutation relations [17, 18]

$$[\hat{e}^{\dagger}_{\alpha'\sigma'}(i'M'), \hat{e}_{\alpha\sigma}(iM)]_+ = \delta_{ii'} \left[\delta_{M',M+\frac{\sigma'-\sigma}{2}} \, |i\alpha'M'\rangle\langle i\alpha M| + \delta_{M',M} \, \delta_{\alpha,\alpha'} \, |i, M - \frac{\sigma}{2}\rangle\langle i, M' - \frac{\sigma'}{2}|\right]. \qquad (2)$$

For sufficiently large J_H, the J=S+1/2 local populations dominate (lower magnetic Hubbard band) and

$$|i\alpha M\rangle = \sqrt{\frac{S+M+\frac{1}{2}}{2S+1}}\ |i\alpha;\uparrow M-\frac{1}{2}\rangle + \sqrt{\frac{S-M+\frac{1}{2}}{2S+1}}\ |i\alpha;\downarrow M+\frac{1}{2}\rangle, \quad (3)$$

where M=$-J\cdots J$ and α labels the eigenstates of the JT and all other local interactions on site i. For our purposes here, the details of these states are not crucial. Assuming that electrons hop between sites faster than the lattice distortions that accompany this hopping, as in the limit $\hbar\omega_{ph}/t \ll 1$ [21], we can approximate $|i\alpha;\sigma/2, M-\sigma/2\rangle \approx c^\dagger_{i\alpha\sigma}\,|i, M-\frac{\sigma}{2}\rangle$, where $c^\dagger_{i\alpha\sigma}$ creates a bare electron with spin $\sigma/2$ in state α ($\sigma=\pm1$). We then project the bare electrons as follows [17]:

$$c^\dagger_{\alpha\sigma i} \approx \hat{e}^\dagger_{\alpha\sigma}(i) = \sum_M F_\sigma(M)\,\hat{e}^\dagger_{\alpha\sigma}(iM), \quad (4)$$

where we introduced the Clebsch–Gordan coefficients

$$F_\sigma(M) = \langle i\alpha M|c^\dagger_{\alpha\sigma i}|iM-\sigma/2\rangle = \sqrt{\frac{S+\frac{1}{2}+\sigma M}{2S+1}}. \quad (5)$$

The projected Hamiltonian reads

$$H(t) = \sum_i\sum_{\alpha M} E_i(\alpha M)\,|i\alpha M\rangle\langle i\alpha M| + \sum_i\sum_m E_i(m)\,|im\rangle\langle im| + H_{hop}(t), \quad (6)$$

where the many–electron states $|i\alpha M\rangle$ and $|im\rangle$ are the eigenstates of the local Mn + O Hamiltonian at site i with eigenvalues $E_i(\alpha M)$ ($|i\alpha M\rangle$) and $E_i(m)$ ($|im\rangle$). The excitation energies

$$\varepsilon_{\alpha\sigma}(i) = E_i(\alpha M) - E_i(M-\frac{\sigma}{2}), \quad (7)$$

depend on the lattice coordinates due to the electron–lattice (JT) local coupling, which lowers the energy of the $|i\alpha M\rangle$ configurations at the JT–distorted bridge sites. We thus assume $\varepsilon_{\alpha\sigma}(i) = -E_{JT}(Q)$ at all bridge sites and $\varepsilon_{\alpha\sigma}(i)=0$ at all corner sites, where Q is the lattice coordinate. The quasi–equilibrium spin directions on each site are determined by the classical spin–canting angles θ_i, which define the local z–axes for spin quantization. The quasi–particle hopping is described by [17]

$$H_{hop}(t) = -\sum_{ii'}\sum_\sigma\sum_{\alpha\alpha'} V_{\alpha\alpha'}(i-i')\left[\cos\left(\frac{\theta_i-\theta_{i'}}{2}\right)\,\hat{e}^\dagger_{\alpha\sigma}(i)\,\hat{e}_{\alpha'\sigma}(i') + \sigma\,\sin\left(\frac{\theta_i-\theta_{i'}}{2}\right)\,\hat{e}^\dagger_{\alpha\sigma}(i)\,\hat{e}_{\alpha'-\sigma}(i')\right], \quad (8)$$

where the hopping amplitudes $V_{\alpha\alpha'}(i-i')$ have both static ($t_{\alpha\alpha'}$) and laser–induced ($\Delta V_{\alpha\alpha'}$) contributions, $V_{\alpha\alpha'}(j-i) = t_{\alpha\alpha'} + \Delta V_{\alpha\alpha'}(t)$. Transient changes in the inter–site hopping amplitudes, ΔV, can arise from the coupling of the optical field:

$$\Delta V_{\alpha\alpha'}(i-j) \approx d_0(t)\,\frac{t_{\alpha\alpha'}(i-j)}{\hbar\omega_p} \quad (9)$$

where d_0(t)=$eE(t)a$ is the Rabi energy, a is the lattice spacing, $E(t)\propto e^{-t^2/t_p^2}$ is the amplitude of the laser field, and $\hbar\omega_p$ is the pump central frequency (t_p=100fs here). Eq. (9) can be derived by expanding the Peierls substitution expression of the hopping amplitude between sites r_i and r_j in terms of the laser vector potential $\mathbf{A}$(t) for typical laser intensities:

$$V_{\alpha\alpha'}(j-i) = t_{\alpha\alpha'}(j-i)\exp[-ie\mathbf{A}(t)\cdot(r_j-r_i)/\hbar c]. \quad (10)$$

$\Delta V(t)$ can also arise from time–dependent changes in the lattice distortions, which change the local configurations. For σ=1, the first term on the rhs of Eq.(8) recovers the double exchange model Hamiltonian [9, 20, 37] and vanishes for anti–parallel spins $|\theta_i$-$\theta_{i'}|$=π.

FEMTOSECOND QUANTUM SPIN DYNAMICS

In this section we discuss the possibility that charge photoexcitation may instantaneously excite spin dynamics. For example, in weakly correlated magnetic semiconductors, a "sudden" non–adiabatic tilt of the magnetization results from photoexcited population of states with strong spin–orbit interaction, which creates a fs spin–orbit–torque pulse [7]. Here we show that fs FM correlation may be induced quasi–instantaneously via quantum spin fluctuations triggered by the photocarriers. The core spin component $S_z(i)$ along the z–axis defined by the quasi–equilibrium spin canting angle θ_i may be expressed in terms of the local populations as follows:

$$S_z(i) = \sum_{m=-S}^{S} m\,\rho_i(m) + \sum_{M=-S-\frac{1}{2}}^{S+\frac{1}{2}} M\,\frac{S}{S+\frac{1}{2}}\sum_\alpha \rho^\alpha_i(M), \quad (11)$$

where

$$\rho_i(m) = \langle|im\rangle\langle im|\rangle, \rho^\alpha_i(M) = \langle|i\alpha M\rangle\langle i\alpha M|\rangle, \quad (12)$$

and we assumed that J_H is sufficiently large so that only J=S+1/2 total spin configurations are populated. Similarly,

the z–component of the itinerant electron spin is expressed as

$$s_z^\alpha(i) = \frac{1}{2S+1} \sum_{M=-S-\frac{1}{2}}^{S+\frac{1}{2}} M\, \rho_i^\alpha(M). \qquad (13)$$

In the classical spin limit, the only populated states have $m = S$ or $M = S + 1/2$, as all spins point along the directions $\theta_i(t)$. Introducing the deviation of $S_z(i)$ from its classical value, $\Delta S_z(i) = S - S_z(i)$, and using the completeness relation

$$\sum_{\alpha M} \rho_i^\alpha(M) + \sum_m \rho_i(m) = 1 \qquad (14)$$

we obtain from Eq.(11)

$$\frac{\Delta S_z(i)}{S} = \sum_\alpha \sum_{M=-S-\frac{1}{2}}^{S-\frac{1}{2}} \frac{S+\frac{1}{2}-M}{S+\frac{1}{2}}\, \rho_i^\alpha(M) + \sum_{m=-S}^{S-1} \frac{S-m}{S}\, \rho_i(m). \qquad (15)$$

The above equation describes canting from the classical spin direction θ_i due to the population of local states with $M \leq S - 1/2$ and $m \leq S - 1$. Similarly, we introduce the deviation of the itinerant electron spin from its classical value, $\Delta s_z^\alpha(i) = \frac{f_i^\alpha}{2} - s_z^\alpha(i)$ where

$$f_i^\alpha = \sum_M \rho_i^\alpha(M), \qquad (16)$$

is the total electron population on site i. We then obtain from Eq.(13)

$$\Delta s_z^\alpha(i) = \frac{1}{2} \sum_{M=-S-\frac{1}{2}}^{S-\frac{1}{2}} \frac{S+\frac{1}{2}-M}{S+\frac{1}{2}} \rho_i^\alpha(M). \qquad (17)$$

In this section we provide an example of photoexcitation of short–range FM correlation $\sum_{i\in I} \Delta S_z(i) \neq 0$ in a cluster I of sites i. To illustrate this possibility, we consider a dimer of AFM local spins that interact with e–h photoexcitations (Fig.1(b)). This dimer consists of (i) a JT–distorted site (site 1) populated by a J=S+1/2 configuration $|i\alpha M\rangle$ with total spin M=S+1/2 and energy $-E_{JT}$, and (ii) an undistorted site (site 2) populated by a core spin S with z–component m=$-S$ anti–parallel to the spin at site 1 and energy zero. A fairly localized charge density [48] already captures some of the properties of the extended system [19, 20, 45] and leads to an effective Hamiltonian with short–ranged interactions [19–21]. Here, such interactions are modified by the coupling of a 100fs optical field pulse with central frequency $\hbar\omega_p \sim E_{JT}$, which drives inter–site charge fluctuations illustrated by yellow arrows in Fig. 1(b). The density matrix of the quantum dimer considered in this section could serve as a quantum variable of a more rigorous density matrix embedding theory that treats strong correlations by mapping the extended system into a self–consistent impurity plus bath problem similar to dynamical mean field theory [49]. Laser–induced non–equilibrium changes in the local density matrix affect the itinerant quasi–particle dispersion, energy bandgap, and phonon properties in correlated systems with "soft" energy bands [8, 50]. In this section we solve the quantum–kinetic equations of motion for the spin–dependent density matrix (appendix) and calculate the z–component of the total core spin of the two above sites, S_z=$S_z(1)$+$S_z(2)$, by using Eq.(11). Fig. 1(c) shows that a finite $\Delta S_z(t)$, Eq.(15), develops with time. A long–range magnetization could then arise if a macroscopic number of dimers (or clusters) orients along a preferred direction [4, 31].

To interpret the calculated time–dependence $\Delta S_z(t)$, we plot in Fig. 2 all photoinduced populations $\Delta\langle|im\rangle\langle im|\rangle$ and $\Delta\langle|i\alpha M\rangle\langle i\alpha M|\rangle$ of the two AFM sites as function of time. Here we assumed the same z–axis for both sites. Figs. 2(a), 2(c), and 2(e) compare the photoexcited spin populations of the JT–distorted site 1 for three short dephasing times T_2 of the inter–site e–h charge fluctuations. The population of the M=S+1/2 ground state configuration decreases with time due to the laser–driven electron hopping to site 2, which creates a quasi–hole excitation $|1\alpha, S{+}1/2\rangle \rightarrow |1S\rangle$ on site 1. This excitation leaves the core spin unchanged with m=S (see lower panels of Figs. 2(a), (c), and (e)), so $\Delta S_z(1) \approx 0$. The photoexcited electron hops on site 2 while conserving spin by creating a local excitation $|2, -S\rangle \rightarrow |2\alpha, -(S-1/2)\rangle$. The population of these $M = -(S-1/2)$ configurations on site 2 results in quantum canting of the local spin $\Delta S_z(2) \neq 0$. For very short dephasing times, the charge fluctuations terminate after the initial charge transfer (see Fig. 2(e) and 2(f) calculated for T_2=8fs). For longer T_2 =50fs, there are additional populations of the M= $S-$1/2 total spin state on site 1 and the $m = -(S-1)$ core spin state on site 2, which further enhance ΔS_z. In this case, the photo–electron can hop back to site 1 from site 2 before the laser–induced inter–site coherence is destroyed, which can lead to non–equilibrium molecular bonding between AFM sites that modifies the inter–site magnetic exchange interaction. Such laser–induced changes in the spin interactions can be described by deriving a quantum master equation from the equations of motion discussed in the appendix. In all cases, charge photoexcitation induces quantum dynamics of $\Delta S_z(t)$, which increases from zero during electron hopping (quasi–instantaneous FM correlation). In our model, $\Delta S_z(t)$ displays a nonlinear dependence on pump intensity due to population inversion with lifetime T_1 (appendix). Singla et. al. [36] observed that pump–probe oscillations in $La_{0.5}Sr_{1.5}MnO_4$ persist at negative time delays (probe before the pump), which is consistent with $T_2 \sim$15fs. For such T_2, Figs 2(c) and (d) show an appreciable FM correlation between the two AFM–coupled sites. In all cases, $\Delta S_z(t)$ describes non–adiabatic dynamics of the background spins, which leads to spin–canting from the quasi–equilibrium directions θ_i that is driven by the photoexcitation of quasi–particles dressed by spin fluctuations as discussed next.

QUANTUM KINETICS OF ITINERANT COMPOSITE FERMION QUASI–PARTICLES

In this section we summarize the equations of motion that determine the energy bands and time evolution of composite fermion quasi–particles in the strong-coupling limit. The time evolution of the local spin–dependent populations $\rho_i^\alpha(M)$ and $\rho_i(m)$ at site i, Eqs. (34) and (35, is determined by the inter–site amplitudes $\langle \hat{e}^\dagger_{\beta\bar{\sigma}}(j)\,\hat{e}_{\alpha\sigma}(i)\rangle$. The equations of motion for the latter non–local coherences, Eq.(36), couple to four–particle density matrices of the form $\langle [\hat{e}^\dagger_{\beta\bar{\sigma}}(j), \hat{e}_{\beta'\sigma'}(j)]_+\, \hat{e}^\dagger_{\alpha'\sigma'}(l)\,\hat{e}_{\alpha\sigma}(i)\rangle$ with $j \neq l, i$. The anti–commutator $[\hat{e}^\dagger_{\beta\bar{\sigma}}(j), \hat{e}_{\beta'\sigma'}(j)]_+$, Eq.(2), differs from its fermionic value due to the restrictions in the population of the J=S+1/2 and J=S-1/2 Hubbard bands imposed by the strong Hund's rule on–site interaction and is determined by the local populations and bosonic excitations. Using a Hartree–Fock factorization of the above four quasi–particle density matrix, we obtain a closed system of equations of motion that takes into account the kinematic interaction due to the strong J_H but neglects fluctuations of the composite fermion anti–commutator:

$$
\begin{aligned}
& i\partial_t \langle \hat{e}^\dagger_{\beta\bar{\sigma}}(j)\,\hat{e}_{\alpha\sigma}(i)\rangle - [\varepsilon_{\alpha\sigma}(i) - \varepsilon_{\beta\bar{\sigma}}(j)]\ \langle \hat{e}^\dagger_{\beta\bar{\sigma}}(j)\,\hat{e}_{\alpha\sigma}(i)\rangle \\
& = \langle [\hat{e}^\dagger_{\beta\bar{\sigma}}(j), \hat{e}_{\beta\bar{\sigma}}(j)]_+\rangle \sum_l \sum_{\alpha'} V_{\alpha'\beta}(l-j)\ \langle \left[\cos\left(\frac{\theta_l-\theta_j}{2}\right)\hat{e}^\dagger_{\alpha'\bar{\sigma}}(l) - \bar{\sigma}\sin\left(\frac{\theta_l-\theta_j}{2}\right)\hat{e}^\dagger_{\alpha'-\bar{\sigma}}(l)\right]\hat{e}_{\alpha\sigma}(i)\rangle \\
& -\langle [\hat{e}^\dagger_{\alpha\sigma}(i), \hat{e}_{\alpha\sigma}(i)]_+\rangle \sum_l \sum_{\beta'} V_{\alpha\beta'}(i-l)\ \langle \hat{e}^\dagger_{\beta\bar{\sigma}}(j)\left[\cos\left(\frac{\theta_l-\theta_i}{2}\right)\hat{e}_{\beta'\sigma}(l) - \sigma\sin\left(\frac{\theta_l-\theta_i}{2}\right)\hat{e}_{\beta'-\sigma}(l)\right]\rangle, \qquad (18)
\end{aligned}
$$

where $i \neq j$. The main difference between composite fermion quasi–particles and bare electrons comes from the spin–dependent anti–commutators

$$
n_{\alpha\sigma}(i) = \langle [\hat{e}^\dagger_{\alpha\sigma'}(i'), \hat{e}_{\alpha\sigma}(i)]_+\rangle = \delta_{ii'}\delta_{\sigma\sigma'}\left[\sum_{M=-S-\frac{1}{2}}^{S+\frac{1}{2}} \frac{S+\frac{1}{2}+\sigma M}{2S+1}\,\rho_i^\alpha(M) + \sum_{m=-S}^{S}\frac{S+\frac{1}{2}+\sigma(m+\frac{\sigma}{2})}{2S+1}\,\rho_i(m)\right], \qquad (19)
$$

where we neglected the population of the $J = S - 1/2$ upper Hubbard band. We note the analogy to the composite boson behavior of excitons, which results in optical nonlinearity [2] due to phase space filling effects arising from the deviation of excitons from bosonic behavior (kinematic interaction). Using the completeness relation Eq.(14) and Eqs.(11) and (13), the above equation takes the following form after neglecting the population of configurations $\alpha' \neq \alpha$:

$$
\begin{aligned}
& n_{\alpha\sigma}(i) = \frac{1}{2S+1}\times \\
& \left[S + \frac{1}{2} + \sigma\left(S_z(i) + s_z^\alpha(i) + \frac{\sigma}{2}\left(1 - f_i^\alpha\right)\right)\right]. \qquad (20)
\end{aligned}
$$

Introducing the spin fluctuations, $\Delta J_z^\alpha(i) = \Delta S_z(i) + \Delta s_z^\alpha(i)$, determined by population of $M \leq S - 1/2$ and $m \leq S - 1$ spin states (see Eqs. (15) and (17)), we obtain from the above equation

$$
\begin{aligned}
n_{\alpha\sigma}(i) = & \frac{S+\frac{1}{2}+\sigma\left(S+\frac{1}{2}-\Delta J_z^\alpha\right)}{2S+1} \\
& + \frac{1-\sigma}{2}\,\frac{1-f_i^\alpha}{2S+1}. \qquad (21)
\end{aligned}
$$

In the limit of classical spins, $S \to \infty$, Eq.(21) gives $n_{\alpha\uparrow}(i) = 1$ and $n_{\alpha\downarrow}(i) = 0$ as in the case of bare electrons. In this approximation, the electrons are effectively spinless, as their spin is locked with the core spin in a FM configuration parallel to θ_i due to Hund's rule [9, 37]. On the other hand, in the case of composite fermions, Eq.(21) gives

$$
n_{\alpha\uparrow}(i) = 1 - \frac{\Delta J_z^\alpha}{2S+1}\ ,\ n_{\alpha\downarrow}(i) = \frac{1-f_i^\alpha+\Delta J_z^\alpha}{2S+1} \neq 0, \qquad (22)
$$

which allows for σ=-1 quasi–particle excitations with total spin anti–parallel to the equilibrium spin direction θ_i. In the above equation, the composite fermion anticommutators depend on the local spin fluctuations ΔJ_z^α, as well as on the filling factor f_i^α that determines the spatial modulation of the local charge.

Eq.(18) suggests a Hubbard–I approximation for describing the itinerant quasi–particles [17, 42]:

$$i\partial_t\,\hat{e}_{\alpha\sigma}(i,t) = \varepsilon_{\alpha\sigma}(i)\,\hat{e}_{\alpha\sigma}(i,t)$$
$$-\langle[\hat{e}^{\dagger}_{\alpha\sigma}(i),\hat{e}_{\alpha\sigma}(i)]_+\rangle\ \sum_l\sum_{\beta'} V_{\alpha\beta'}(i-l)\ \left[\cos\left(\frac{\theta_l-\theta_i}{2}\right)\hat{e}_{\beta'\sigma}(l,t) - \sigma\sin\left(\frac{\theta_l-\theta_i}{2}\right)\hat{e}_{\beta'-\sigma}(l,t)\right]. \quad (23)$$

For a periodic lattice of sites located at positions (R,i), where i now labels the different atoms in the unit cell and R is the periodic lattice vector, we transform to k–space,

$$\hat{e}_{k\sigma}(i\alpha) = \frac{1}{\sqrt{N}}\sum_R e^{-ikR}\,\hat{e}_{\alpha\sigma}(Ri), \quad (24)$$

where N is the number of unit cells and k is the wavevector, and introduce the normal modes

$$\hat{e}_{nk} = \sum_{i\beta\sigma} u^{\sigma}_{nk}(i\alpha)\frac{\hat{e}_{k\sigma}(i\beta)}{\sqrt{n_{\beta\sigma}(i)}}, \quad (25)$$

where n labels the different quasi–particle branches (bands). From Eq. (23) we then obtain the following eigenvalue equation, which describes the quasi–particle energy bands:

$$(\omega_{nk}-\varepsilon_{\beta\sigma}(j))\,u^{\sigma}_{nk}(j\beta) = -\sum_{l\alpha} V^k_{\alpha\beta}(l-j)\,\sqrt{n_{\beta\sigma}(j)}\,\sqrt{n_{\alpha\sigma}(l)}\,\cos\left(\frac{\theta_l-\theta_j}{2}\right)u^{\sigma}_{nk}(l\alpha)$$
$$+\sigma\sum_{l\alpha} V^k_{\alpha\beta}(l-j)\,\sqrt{n_{\beta\sigma}(j)}\,\sqrt{n_{\alpha-\sigma}(l)}\,\sin\left(\frac{\theta_l-\theta_j}{2}\right)u^{-\sigma}_{nk}(l\alpha). \quad (26)$$

where

$$V^k_{\alpha\beta}(i-j) = \sum_R V_{\alpha\beta}(R+i-j)\,e^{-ikR}, \quad (27)$$

The above eigenvalue equation depends on the coupling between σ=1 (parallel quasi–particle spin) and σ=-1 (anti–parallel quasi–particle spin) excitations. By neglecting this coupling, the σ=1 contribution to the above equation recovers the previous results for bare electrons and classical spins [9, 20, 37, 53]. In this case, the quasi–particle excitation total spin is locked parallel to the background spins throughout the motion and its hopping amplitudes $V^k_{\alpha\beta}(l-j)\,\sqrt{n_{\beta\uparrow}(j)n_{\alpha\uparrow}(l)}\cos\left(\frac{\theta_l-\theta_j}{2}\right)$ are maximized between FM sites with θ_i=θ_j. On the other hand, for quantum spins, the finite anticommutator $n_{\alpha\downarrow}(i)$ couples σ=1 and σ=-1 excitations and allows composite fermion quasi–particles to hop between AFM sites $|\theta_l-\theta_j|\sim\pi$ with an amplitude $V^k_{\alpha\beta}(l-j)\,\sqrt{n_{\beta\uparrow}(j)n_{\alpha\downarrow}(l)}\sin\left(\frac{\theta_l-\theta_j}{2}\right)$. In this way, the quantum spin fluctuations couple the AFM chains and planes of Fig. 1(a) (second term on the rhs of Eq.(26)) and lead to quasi–particle delocalization.

Eq.(26) describes "soft" energy bands of itinerant composite fermion quasi–particles. These bands depend non–perturbatively on the local spin and charge populations of the different lattice sites as determined by Eqs. (19) and (22). This dependence on the itinerant quasi–particle dispersion on the local density matrix, due to the deviations of the composite fermions from fermionic behavior, can lead to laser–induced non–adiabatic changes determined by the equations of motion Eqs. (34) and (35). In addition, the quasi–particle energy bands depend on the background spins via the classical spin–canting angles $\theta_i(t)$. Finally, they depend on the classical lattice displacements and their dynamics, which determine the eigenstates $|i\alpha M\rangle$ and $|im\rangle$ of the local Hamiltonian on each lattice site. This local Hamiltonian changes with lattice motion, which leads to lattice–dependent local excitation energies $\varepsilon_{\alpha\sigma}(i)$, Eq. (7), and hopping matrix elements $V_{\alpha\alpha'}$. In the next sections we discuss the possible role of the "soft" quasi–particle energy bands Eq.(26) in photo–induced phase transitions and note that analogous laser–induced quasi–particle changes in $TiSe_2$, VO_2, and Ga(Mn)As systems have been discussed in Refs. 7, 8, and 50.

PROPERTIES OF ITINERANT QUASI–PARTICLE BANDS

In this section we compare the energy dispersions between bare electrons and composite fermion quasi–particles. We consider a periodic system with the CE–AFM unit cell, Fig. 1(a), with 16 sites as discussed in Section II (two bridge and two corner sites per chain, two AFM chains per plane, two

AFM planes). Similar results are obtained for other AFM unit cells. For bare electrons, $n_{\alpha\uparrow}$=1 and $n_{\alpha\downarrow}$=0, so electron hopping between sites i and j located in different chains can only occur with finite canting of the spin background, $|\theta_i - \theta_j| \neq \pi$. In this section we consider excitation of a collinear AFM background state, so θ_i=0 or θ_i=π. For composite fermions, the hopping amplitudes in Eq.(26) depend on the anti–commutators $n_{\alpha\sigma}(i)$, Eq.(22). In this section we assume background spins relaxed along θ_i, so ΔJ_z=0. The difference between composite fermion and bare electron bands then comes from the finite $n_{\alpha\downarrow}(i)$ on sites with total charge $f_i^\alpha < 1$, which allows hopping between AFM planes and chains. In order to compare with the results of Refs. [9, 20], we use the same tight–binding parameters. Our conclusions about the effects of the finite $n_{\alpha\downarrow}(i)$ do not rely on the exact charge modulation f_i^α or parameter values, so we follow Ref. [44] and simply assume that only the lowest energy Mn + O configuration α is populated in the bridge sites, f_i^α=1, while only S=3/2 spin Mn + O configurations are populated in the corner sites, f_i^α=0. Similar results are however obtained for different charge density modulations f_i^α, which can be included phenomenologically [15] or calculated self–consistently in equilibrium using an ab–initio theory for the local multi–electron configurations.

Fig. 3 compares the calculated quasi–particle dispersions along the three different directions marked in Fig. 1(a): k_x (along the zig–zag chains), k_y (perpendicular to the chains but along the same plane), and k_z (perpendicular to the planes). For a collinear AFM state, there are pronounced differences in the energy bands between bare electrons ($n_{\alpha\uparrow}(i) = 1$ and $n_{\alpha\downarrow}(i) = 0$) and composite fermion quasi–particles ($n_{\alpha\uparrow}(i) = 1$ but $n_{\alpha\downarrow}(i) \neq 0$). This is the case for both small (Figs 3(a) and (b)) and large (Figs 3(c) and (d)) JT energy barrier E_{JT} between the bridge and corner sites. Figs. 3(a) and 3(c) also show a pronounced difference between the e (above the insulator gap) and h (below the insulator gap) energy bands for quantum spins, which differ markedly from the case of classical collinear AFM spins (Figs. 3(b) and 3(d)).

In the classical spin limit, Figs 3(b) and 3(d) show that there is no energy dispersion along k_y and k_z, as electron hopping between different AFM–coupled chains and planes is prohibited without spin canting between chains. The only energy dispersion comes from electron motion along a single chain with FM spins [9, 53]. For large E_{JT}, this k_x–dispersion is also small, due to the energy barrier E_{JT} between the alternating JT–distorted and undistorted sites observed experimentally [20, 44, 52]. Therefore, the electron charge density is mostly localized in all three directions for large E_{JT}. This justifies the use of a localized electron effective Hamiltonian for describing the spin interactions [20, 21], as in the previous section. With decreasing E_{JT}, the k_x dispersion increases, determined by the ratio t/E_{JT}. However, the energy bands below and above the energy gap have a similar dispersion (Fig. 3(b)), which can be obtained analytically [20]. Importantly, the lowest conduction band is dispersionless [9] and is a linear combination of corner state configurations [20]. The insulator energy gap corresponds to transitions from the valence band and the above discrete state [20].

As seen in Fig. 3, the above picture changes when spin fluctuations are included non–perturbatively by using Eq. (26). This is already seen in the deep insulating limit of large E_{JT}, where the JT confinement results in energies clustered around ε=0 (undistorted sites) and ε=-E_{JT} (JT–distorted sites) (see Figs. 3(c) and (d)). The energy gap is then dominated by E_{JT}, so a transition to a metallic state requires relaxation of the JT distortions. However, the JT confinement does not prohibit tunneling between stacked planes (see Fig. 1(a)), which are AFM–coupled. With quantum spin fluctuations, Fig. 3(c) shows that a finite quasi–particle energy dispersion develops in the conduction band along k_z, due to deformation of the collinear AFM background by the excited electrons. In this case, quasi–particle excitation opens up a channel of inter–plane hopping, which delocalizes the electrons via quantum spin fluctuations (electron–magnon coupling).

Figs. 3(a) and 3(b) show that the differences in the energy bands between a bare electron and a composite fermion quasi–particle become very pronounced as $E_{JT} \sim t$. On the other hand, the valence bands remain similar. First, there are multiple composite fermion conduction bands that disperse in all three directions, as both in–plane and out–of–plane electron hopping between AFM chains is now facilitated by the quantum spin fluctuations and can overcome the JT confinement as E_{JT} decreases. Second, the delocalization between the AFM chains, enabled by the finite $n_{\alpha\downarrow}(i)$, significantly decreases the insulator energy gap (factor of two difference in Fig 3) as compared to the case of an adiabatically–decoupled classical spin background that is assumed to be slower than electron hopping. This result suggests that, as the JT confinement decreases, the excitation of composite fermion quasi–particles can quench the insulator gap via quasi–instantaneous spin fluctuations in the excited state. The non–perturbative charge–spin coupling thus favors an insulator–to–metal transition. Excitation of a degenerate population of quasi–electrons increases the spin canting and can in this way induce metallic behavior, discussed in the next section. Note that classical spin calculations generally produce critical magnetic fields that are much larger than the values measured in experiment, as they require a large canting of the average background spins to be induced by an external field in order to obtain metallic behavior [20]. On the other hand, quantum spin canting is induced instantaneously by the excited composite fermion quasi–particles, whose population can be controlled by laser photoexcitation.

Fig. 4 shows more directly that the composite fermion quasi–electron excitations of the extended AFM system are accompanied by strong quantum spin canting of the collinear CE–AFM state. To see this, we compare the probabilities $\sum_{j\beta} |u^n_{k\uparrow}(j\beta)|^2$ and $\sum_{j\beta} |u^n_{k\downarrow}(j\beta)|^2$ that describe the spin mixing as function of E_{JT} for two eigenstates with k=0, below (left panel) and above (right panel) the insulator gap. σ=1 (σ=-1) means quasi–particle total spin parallel (anti–parallel) to the background local spin equilibrium direction.

For bare electrons and classical spins, $\sum_{j\beta} |u^n_{k\uparrow}(j\beta)|^2$=1 and $u^n_{k\downarrow}(j\beta)$=0. This is the case when there is no deformation of the background spins with respect to the quasi–equilibrium local canting angles θ_i (adiabatic decoupling of the spin background from the electronic hopping motion). In Fig. 4, the eigenstate below the energy gap has very small quantum spin canting, only for $E_{JT} \leq t$ ($u^n_{k\downarrow}(j\beta) \approx$0 in the left panel of Fig. 4). Therefore, the motion of a quasi–hole mostly occurs within a single FM chain and does not induce strong spin dynamics. In contrast, the right panel of Fig 4 shows that a pronounced spin deformation is induced by quasi–electron excitations above the insulator energy gap during the electronic hopping. This is witnessed by the large probability of spin–flips over a wide range of E_{JT} for such eigenstates: $\sum_{j\beta} |u^n_{k\downarrow}(j\beta)|^2 \approx \sum_{j\beta} |u^n_{k\uparrow}(j\beta)|^2$. We therefore expect that a population of composite fermion quasi–electrons excited above the insulator gap will instantaneously deform the anti–parallel background spins and thus induce FM correlation already during excitation. With increasing quasi–particle density, these spin deformations will multiply. They can already induced during fs laser excitation, either directly by the coupling of the optical field (Section VIII) or via a fast avalanche effect that excites many composite fermion e–h pairs close to the insulator gap during the relaxation of a photoexcited high energy pair [8]. In the next section we discuss the possible implication of the above results for non–equilibrium phase transitions driven by laser–induced spin canting.

EFFECTS OF SPIN AND LATTICE PHOTOEXCITATION

In this section we propose a mechanism that can lead to a photoinduced insulator to metal transition driven by laser–induced spin canting and lattice motion. Similar to previous works, we assume that the lattice motion can be described by classical coordinates Q [9, 20, 21]. The eigenstates $|i\alpha M\rangle$ of the local Hamiltonian depend on Q due to electron–lattice coupling, which we model by introducing a linear Q–dependence of the energy eigenvalues $E_i(\alpha M)$ similar to Refs. 9 and 46. We neglect any Q–dependent changes in the hopping parameters, which are less known in the real materials [19] and should enhance the predicted effect.

Fig.5 shows the dependence of the low energy quasi–particle energy bands on the energy barrier $E_{JT}(Q) = \varepsilon_{JT} Q$ induced by the local electron–lattice coupling. These results were obtained with a real space calculation of a small system with periodic boundary conditions, which converges for sufficiently large system size along the z–axis and reproduces the results obtained in the periodic system. Fig. 5 compares the Q–dependence of the energy bands between bare electrons, which move on top of an adiabatically–decoupled classical spin background (upper panel), and composite fermion quasi–particles, whose motion deforms the background spins via electron–magnon strong coupling (lower panel). It demonstrates that the conduction and valence bands have different dependence on both lattice distortions and spin fluctuations. For classical spins, the upper panel of Fig. 5 reproduces previous results [20]. For collinear CE–AFM order, θ=0, in this case the energy gap does not close even for undistorted lattice Q=0, due to the electronic order of a single zig–zag chain [9, 20]. As can be seen analytically [20], the unit cell of a single zig–zag chain with four inequivalent bridge and corenr sites results in two kinds of bands. The Q–dependent energy bands are linear combinations of the local configurations of bridge and corner sites. These bands, whose dispersion in the first Brillouin zone is shown in Fig. 3, determine the Q–dependence of both ground state energy and hole quasi–particle energies. In addition, Fig. 5(a) shows a discrete degenerate state with energy $\varepsilon = 0$. In the case of classical spins, this lowest conduction band state is a linear superposition of the electronic configurations in the two different corner sites of the zig–zag chain unit cell and thus does not depend on Q [20]. With increasing spin canting angle θ between the chains, electronic hopping between planes breaks the degeneracy of the above ε=0 state, which broadens the lowest conduction band [20]. For large FM correlation between the chains, this bandwidth increases and the energy gap closes, which results in metallic behavior induced by a large classical spin canting $\theta \geq 15^o$.

In contrast to the above classical spin results, the lower panel of Fig. 5 shows that, with $n_\downarrow \neq 0$, the conduction band of composite fermion quasi–particles is already very broad and metallic in the collinear AFM ground state θ=0. Such metallic conduction band arises from the quantum spin canting induced by the excitation of the quasi–electron, which can tunnel between the different AFM planes and chains due to electron–magnon quantum fluctuations that cant the background spins. While treating the spin background as adiabatic assumes that it is slower than the electronic hopping, for composite fermions quantum spin canting occurs during electronic hopping timescales. This results in instantaneous metallic behavior and FM correlation during quasi–particle excitation, even for large Q. As seen in Fig. 5(d), this can quench the energy gap even prior to any increase in θ. With increasing FM correlation between the chains, $\theta > 0$, the value of the critical lattice distortion $Q_c > 0$ below which the energy gap closes increases. Figs. 5(d), (e), and (f) suggest that an insulator to metal transition will occur when $Q \leq Q_c$. The existence of two kinds bands with different dependence on the lattice and spin degrees of freedom is consistent with previous descriptions of the equilibrium states and CMR phase transition of AFM insulating manganites in terms of polaronic majority carriers and metallic–like minority carriers [21, 24].

In the ground state, the system is insulating, so $Q > Q_c$. Assuming $\theta \sim 0$ as seen in experiments, Q_c=0 in the case of

classical spins, as the electronic order of a zig–zag chain maintains the energy gap even for Q=0. For composite fermions, the spin fluctuations quench the electronic energy gap, so a larger lattice displacement is required to maintain it, $Q_c \geq 0$. Laser excitation can lead to $Q(t) \leq Q_c(t)$ and thus induce an insulator–to–metal transition in two different ways: (i) increase $Q_c(t) > Q_c$, (ii) decrease $Q(t) < Q$ as compared to the ground state. Fig. 6 demonstrates the difference in the Q–dependence of the e–h quasi–particle energy gap extracted from Fig. 5 between composite fermion and bare electron excitations. It also shows that spin canting $\theta > 0$ increases the critical lattice displacement Q_c required to maintain an energy gap. In the case of bare electrons, Fig. 6(a), the energy gap does not close down to $Q = 0$ without a large canting angle θ between the AFM chains. On the other hand, for composite fermions, Fig. 6(b) shows that quantum spin canting during quasi–particle excitation softens the energy gap, which now closes below $Q_c \geq 0$ even for θ=0. The critical value Q_c increases with background spin canting θ for both classical and quantum spins. However, in the case of bare electrons with adiabatically–decoupled slower spins and more "rigid" quasi–particle bands, a large spin canting angle θ is required for Q_c to become comparable to that in the case of composite fermions with "soft" energy bands. As a result, the insulating state is more robust and rigid in the case of classical adiabatically–decoupled spins, so it is more difficult to photoinduce a phase transition without spin canting.

Furthermore, Fig. 6(c) shows that, in the case of composite fermions, the charge excitation gap depends on the spin fluctuations around the average direction $\theta_i(t)$ via $\Delta J_z(i) = \Delta S_z(i) + \Delta s_z(i)$ Eqs. (15) and (17), which determine the composite fermion anti–commutator. Such spin fluctuations can be induced by photoexcitation of local spin populations with $M \leq S - 1/2$ and $m \leq S - 1$, analogous e.g. to Section III or via an ultrafast avalanche effect that excites many quasi–particles during relaxation of the high–energy photocarriers. This results in time–dependent changes of the composite fermion anti–commutator Eq.(22) and thus to quasi–instantaneous non–perturbative changes in the quasi–particle properties and energy dispersion, obtained from Eqs.(22) and (26):

$$\Delta n_{\alpha\sigma}(i) = -\frac{\sigma \Delta J_z^{\alpha}(i) + \frac{1-\sigma}{2}\Delta f_i^{\alpha}}{2S+1} \qquad (28)$$

The dependence of the composite fermion anti–commutator $n_{\alpha\downarrow}(i)$ on the spin fluctuations $\Delta J_z^{\alpha}(i)$ results in a dynamic change of the "soft" quasi–particle energy bands during time evolution of the spin populations and local density matrix, determined by the equations of motion Eqs.(35) and (34). An example of quasi–instantaneous change in $\Delta J_z(t)$ due to quasi–particle charge excitation by the coupling of an optical field pulse was given in Section III. $\Delta J_z(t)$ may also be induced during the initial stage of photocarrier relaxation via excitation of e–h quasi–particles dressed by quantum spin fluctuations in the presence of a small magnetic field that introduces a preferred direction. In all cases, photoexcitation of $\Delta J_z^{\alpha}(i) > 0$ increases $n_{\alpha\downarrow}(i)$, which instantaneously quenches the energy gap and increases $Q_c(t)$ as shown in Fig. 6(c). We conclude that, independent of the details of fs spin photogeneration, both adiabatic $\theta(t) > 0$ and nonadiabatic $\Delta J_z(t) > 0$ FM correlation induced by the photoexcitation leads to increased $Q_c(t)$. Such FM correlation during 100fs timescales is observed experimentally above a pump fluence threshold [4] and can trigger a metal to insulator transition if it is sufficient for $Q(t) \leq Q_c(t)$. This may already occur during photoexcitation of sufficient population of composite fermion quasi–particles, which can leads to instantaneous FM correlation as discussed above. However, the detailed time–dependence of the photoinduced spin canting, which determines the critical photocarrier density such that $Q(t) < Q_c(t)$ as required for a phase transition, is beyond the scope of the present paper and will differ in different materials. Independent of whether the condition $Q(t) < Q_c(t)$ is reached or not following laser excitation, Fig. 6 implies a nonlinear dependence of the electronic properties on the pump fluence, as the latter controls the non–thermal populations of the composite fermion excitations that "suddenly" change the "soft" energy bands and Q_c, while also inducing lattice displacements $Q(t) < Q$ as discussed next. We expect that, with multiple quasi–particle excitations, such nonlinear dependence will be even stronger than the single quasi–particle results presented here. We note that classical spin equilibrium calculations [20] predict a very high critical magnetic field for inducing a CMR phase transition, due to the large charge excitation energy gap for adiabatically–decoupled spins. Here we argue that composite fermion excitations characterized by "soft" energy bands that can be manipulated optically can make an insulator to metal and AFM to FM transition possible for low magnetic fields and pump fluences.

The second pathway in which optical excitation can lead to an insulator to metal transition is to reduce the lattice displacement $Q(t)$ from its equilibrium value Q. The effective potential that governs the lattice motion $Q(t)$ includes both the classical contribution $U_L(Q)$, which can be obtained phenomenologically based on the symmetry [28, 54], and the contribution of the local electron–lattice coupling. The latter is important for the laser–induced phase transition proposed here and is described by the Q–dependence of the Hamiltonian Eq.(6). The lattice equations of motion can be derived as in Ref. 55. For this we introduce an orthonormal basis of many–electron states $|n>$ and expand the time–dependent many–body state $|\Psi(t)\rangle$ evolving from the equilibrium state $|G\rangle$ following photoexcitation. The time–dependence of the lattice coordinates is described by the classical equation of motion $M_l \frac{d^2 Q_l}{dt^2} = F_l(Q)$, where the forces are determined by the electronic density matrix $\rho_{n'n}(t) = \langle n'||\Psi(t)\rangle\langle\Psi(t)||n\rangle$ [55]:

$$F_l = -\frac{\partial}{\partial Q_l}\left[U_L(Q) + \sum_{nn'} \rho_{n'n}(t) < n|H(Q,t)|n'\rangle\right] \qquad (29)$$

After the laser pulse, the off–diagonal density matrix ele-

ments can be neglected by assuming rapid dephasing. Using the many–body eigenstates of $H(Q)$ as basis and separating the contributions of the equilibrium state $|G\rangle$ from the continuum of excited states $|E\rangle$ shown in Fig. 5, we obtain from the above equation after using the completeness of the basis states and introducing the time–dependent populations $f_E(t) = \rho_{EE}(t)$ of the many–body states

$$F_l(Q,t) \approx -\frac{\partial}{\partial Q_l}\ [U_L(Q) + \langle G|H(Q)|G\rangle] - \sum_{E\neq G} f_E(t)\ \frac{\partial \varepsilon_E(Q)}{\partial Q_l}, \tag{30}$$

where

$$\varepsilon_E(Q) = \langle E|H(Q)|E\rangle - \langle G|H(Q)|G\rangle \tag{31}$$

are the e–h quasi–particle excitation energies as in Fig. 5, which depend on $Q(t)$. The first term on the rhs of Eq.(30) gives the adiabatic potential, which determines the lattice motion in the case of adiabatic time evolution of the insulating state $|G\rangle$ without quasi–particle excitation [26]. The second term on the rhs of Eq.(30) describes a quasi–instantaneous change in the lattice potential and forces from their quasi–equilibrium values when the population of excited many–body states $|E\rangle$ becomes significant. Such non–equilibrium potential change initiates lattice motion following quasi–particle excitation and changes with time as determined by the evolution of the non–equilibrium populations $f_E(t)$ and by the dependence of the excitation energies Eq.(31) on $Q(t)$. This is analogous to previous results in VO_2 [50, 51] and semiconductors [56]. A phase transition is triggered if $Q(t) \leq Q_c(t)$ during the lattice motion $Q(t)$, where the latter can involve coherent phonon oscillations and/or anharmonic damped motion. Fig. 5 indicates a nonlinear Q–dependence of both ground state energy and e–h quasi–particle excitation energies consistent with previous classical spin results [20]. As a result, Eq.(30) implies that the effective spring constants which determine, e.g., the coherent phonon oscillation frequencies, will change from their quasi–equilibrium values following photoexcitation of $f_E(t)$ even without any phase transition. On the other hand, for $E_{JT}(Q) \gg t$, the energy band Q–dependence is approximately linear, which implies much smaller changes in the sping constants. The fs–resolved XRD experimental results of Ref. 28 show that the photocarrier density transiently modifies the lattice spring constants in the manganites, consistent with the above results.

The laser–induced changes in the lattice potential and forces with quasi–particle excitation will initiate a lattice motion that depends on both $f_E(t)$ and $\frac{\partial \varepsilon_E(Q)}{\partial Q}$. New metastable quasi–equilibrium lattice configurations $Q_{eq}(t)$ can be obtained from Eq.(30) by setting $F_l(Q) = 0$. Such configurations depend on the elastic potential $U_L(Q)$, determined by multiple lattice modes and lattice anharmonicities [26, 54]. For our purposes here, we assume a simple $U_L(Q) = \frac{1}{2}kQ^2$. In this case, Eq.(30) gives quasi–equilibrium lattice configurations that depend on the photocarrier density:

$$Q_{eq}(t) = -\frac{1}{k}\frac{\partial}{\partial Q}\langle G|H(Q)|G\rangle - \frac{1}{k}\sum_{E\neq G} f_E(t)\ \frac{\partial \varepsilon_E(Q)}{\partial Q}. \tag{32}$$

The first term determines the quasi–equilibrium lattice distortions, which are however modified following photoexcitation of the continuum of many–body states $|E\rangle$. From Fig. 5 we see that $\frac{\partial \varepsilon_E(Q)}{\partial Q} > 0$ is dominated by the hole contribution to the excitation energy. The photoexcited quasi–particle populations then decrease the quasi–equilibrium lattice displacements to $Q_{eq}(t) < Q$ when $f_E(t) \neq 0$.

The lattice displacements $Q_{eq}(t)$ are expected to be small, $Q_{eq}(t) \ll Q$, in the case of laser–induced population inversion between the two different quasi–particle bands of Fig. 5. This is the case as the conduction and valence band eigenstates have different admixture of corner and bridge site configurations, which leads to their different Q–dependence, and may lead to an irreversible transition when $Q_{eq}(t) \leq Q_c(t)$. Noting that $\frac{\partial \langle n|H(Q)|n\rangle}{\partial Q} = \langle n|\frac{\partial H(Q)}{\partial Q}|n\rangle$ for the many–body eigenstates of the Hamiltonian $H(Q)$, we obtain from Eq.(32) after assuming for simplicity that the Q–dependence of the Hamiltonian Eq.(6) mainly comes from the energies $E_i(\alpha M)$

$$Q_{eq}(t) \approx -\frac{1}{k}\sum_{i\alpha M}\frac{\partial E_i(\alpha M)}{\partial Q}\left[\langle G||i\alpha M\rangle\langle i\alpha M||G\rangle\left(1 - \sum_{E\neq G} f_E(t)\right) + \sum_{E\neq G} f_E(t)\langle E||i\alpha M\rangle\langle i\alpha M||E\rangle\right]. \tag{33}$$

As the energy gap closes, the population of the excited state metallic continuum $|E\rangle$ (lower panel of Fig. 5) increases, $\sum_{E\neq G} f_E(t) \sim 1$, and the lattice displacements are determined by the populations of the JT–distorted sites in the continuum of excited states $|E\rangle$. For multiple e–h quasi–particle excitations during the fast relaxation of an initial photoexcited high energy e–h, the population of lattice–distorted bridge site configurations $|i\alpha M\rangle$ in the highly excited many–body states $|E\rangle$ is expected to be small. Therefore, the quenching of the insulator energy gap by the spin fluctuations facilitiates a quasi–equilibrium lattice structure with small JT displacements due to the differences between the polaronic valence band and the broad metallic conduction band.

The above picture of a photoinduced insulator to metal tran-

sition above a critical photocarrier density such that $Q(t) \leq Q_c(t)$ may be validated by experimental observations of nonlinear and threshold dependences of the ultrafast spectroscopy signals with increasing pump fluence and with a better temporal resolution of fs XRD that can distinguish between instantaneous and time–delayed processes. In the non–thermal temporal regime of interest here, a laser–induced population inversion between the polaronic–like majority carriers and the metallic–like minority carriers drives a nonlinear inter–dependence of spin, charge, and lattice dynamics. In this way, fs laser excitation can break the balance between electronic/magnetic and lattice degrees of freedom based on their different dynamics as discussed above. To test this picture experimentally, one must be able to non–thermally control the quasi–particle populations while simultaneously monitoring the resulting spin, charge, and lattice time evolution on a fs timescale. This may be possible by using fs X–ray pulses [28, 34] as their time resolution improves. Several experimental results so far, discussed in the introduction, indicate the importance of AFM order and nonlinearity in the non–thermal fs temporal regime, consistent with our predictions here. In the next section we present pump–probe differential reflectivity and magneto–optical simultaneous measurements that show a non–linear threshold pump fluence dependence of both the spin and the charge dynamics measured during $\sim$100fs timescales.

EXPERIMENTAL RESULTS AND THEIR RELATION TO THE THEORY

In this section we present femtosecond pump–probe differential reflectivity and magneto–optical spectroscopy experimental results showing nonlinear pump fluence threshold dependence below the transition temperature for AFM order. We studied $Pr_{0.7}Ca_{0.3}MnO_3$ (PCMO) single-crystals grown by the floating–zone method. An important characteristic of this narrow-bandwidth manganite is that all its equilibrium phases are insulating. CO/OO electronic order sets in below $\sim$200K, while CE–AFM order sets in below $\sim$140K. We used a Ti:Sapphire amplifier laser beam with pulse duration of 35fs and repetition rate of 1KHz to perform *fs* pump–probe spectroscopy measurements of the differential reflectivity $\Delta R/R$, magneto-optical Kerr effect (MOKE, $\Delta\theta_k$), and magnetic circular dichroism (MCD, $\Delta\eta_k$) signals. In this way, we can compare the fs and ps spin and charge dynamics. To break the symmetry, we applied a small magnetic field B$\leq$ 0.25T, much smaller than the critical field required for CMR transition, which introduces a preferred direction perpendicular to the sample surface.

Fig.7(a) shows the *fs*–resolved $\Delta R(t)/R$ signal measured at 30K when both pump and probe are tuned at 1.55eV. For relatively high pump fluences $\sim$4.9 mJ/cm^2, we observe a bi–exponential ultrafast relaxation with two distinct signal decay times, $\tau^{\rm fs}\sim$530fs and $\tau^{\rm ps}\sim$5.7ps. As seen by comparing the normalized $\Delta R/R$ traces, this two–component relaxation is suppressed for low–fluences (Fig. 7(b)) or/and for high temperatures (Fig. 7(c)). At low temperature (30K), the two relaxation components are observed even for low pump fluence, but the temporal profile of the normalized $\Delta R/R$ differs between low 0.4 mJ/cm^2 and high 6.2 mJ/cm^2 pump fluence (Fig. 7(b)). In particular, for 0.4 mJ/cm^2 fluence, the amplitude of the $\tau^{\rm fs}$ component is much smaller than that of the $\tau^{\rm ps}$ component, while this reverses for high photoexcitation intensity. On the other hand, at high temperatures ($\sim$300K) above the critical temperatures for CO/OO (200K) and AFM (140K) phase transitions, Fig. 7(c) shows that all pump fluences give the same single–exponential decay, with a relaxation time $\tau^{\rm ini}$ that is much shorter than both $\tau^{\rm fs}$ and $\tau^{\rm ps}$. This drastic change in the temporal profile of $\Delta R/R$ with increasing temperature indicates that the bi–exponential relaxation is related to the electronic and/or magnetic order. To clarify this, Figs. 8(a) and 8(b) show the detailed temperature dependence of the two–step pump–probe signal recovery at high pump fluence (6.2 mJ/cm^2). The two relaxation components $\tau^{\rm fs}$ and $\tau^{\rm ps}$ appear below T=140K, i.e., below the AFM phase transition (Neel) temperature. We conclude from the above that the observed bi–exponential relaxation is mainly related to AFM order.

Fig. 9 shows a 2D false color plot of $\Delta R/R$ as function of pump–fluence and time delay for two probe frequencies. The color gradients demonstrate clear differences, along both axes, between probe frequencies close to [1.55 eV, Fig. 9(a)] or far above [3.1 eV, Fig. 9(d)] the insulator energy gap. While at 1.55eV the peak of $\Delta R(t)/R$ shows an almost linear fluence–dependence, as expected from photo–carrier populations [56], at 3.1eV it displays a transition from linear to nonlinear saturation with increasing intensity. The pump photon frequency was kept at $\hbar\omega_p$=1.55eV (800nm) for both probe frequencies, so the pump excites photo–carriers near the insulator gap and is far detuned from the phonon frequencies. For 1.55 eV probe, the amplitude of the photoinduced $\Delta R/R$ in the non–thermal temporal regime is expected to reflect the laser–excited quasi–particle density and temperature, which also determine the lattice displacements [56]. We do not observe any coherent phonon oscillations in $\Delta R/R$, perhaps due to the time resolution ($\sim$100fs pulses are longer than the $\sim$70fs JT phonon period) or due to strong phonon damping and nonlinearity induced by the photocarriers. Similar to other experiments discussed in the introduction, we interpret our observation of two distinct relaxation times $\tau^{\rm fs}$ and $\tau^{\rm ps}$ in the AFM–ordered state to reflect the dynamics of non–thermal electronic and spin populations of excited states ($\tau^{\rm fs}$) and quasi–equilibrium lattice relaxation ($\tau^{\rm ps}$), respectively.

The differential reflectivity signal $\Delta R(t)/R$ measured at 3.1eV does not show any bi–exponential relaxation following 1.55eV pump photoexcitation. We expect that the "sudden" increase of this non–resonant $\Delta R/R$ signal during $\sim$100fs time delays mainly reflects a "sudden" increase and saturation of the overall conductivity of the photoexcited system. Such behavior is expected, e.g., from an ultrafast quench of the electronic component of the insulator energy gap [8] as

in our theory. Following the rapid fs rise, Fig. 9(f) shows a slower *ps* increase of $\Delta R(t)/R$, which is consistent with the expected increase in conductivity due to quasi–equilibrium lattice structure relaxation. The possible connection between spin and charge dynamics during fs non–thermal timescales can be elucidated by comparing the pump fluence dependence of the amplitudes of the two $\Delta R/R$ relaxation components observed at 1.55eV to that of the fs–resolved MCD and MOKE signals ΔM. The latter magneto–optical signals measured at time delays of 200fs or earlier at probe frequencies 3.1eV far detuned from the 1.55eV pump are shown in Fig 10. Fig. 10(a) shows clearly that *both* MOKE and MCD signals have the *same* pump–fluence–threshold nonlinear behavior at 200fs for very small magnetic field. The observation of a threshold nonlinearity is typically considered as a signal of a non–equilibrium phase transition. Here, the nonlinear increase of both MOKE and MCD at ∼200fs, above a phototoexcitation intensity threshold ∼2–3 mJ/cm^2, indicates that, above a critical photocarrier density, laser–induced FM correlation develops on a ∼100fs timescale or less. In particular, the appearance of the same quasi–instantaneous jump in both MOKE and MCD fs signals (inset of Fig. 10(a)) for magnetic field ∼250mT well below the critical field required for AFM→FM phase transition and CMR in equilibrium (few Tesla) indicates the observation of *fs* magnetization photogeneration coming from charge photoexcitation. Such laser–induced FM correlation at 100fs timescales only occurs above a critical pump–fluence of 2-3mJ/cm^2 (compare the two temporal profiles in the inset above and below the pump fluence threshold for $\Delta M > 0$ seen in Fig. 10(a)), which indicates that a sufficiently large non–thermal photocarrier population is necessary. This threshold nonlinearity of ΔM with increasing pump fluence is absent at ps time delays, which are governed by quasi–thermal lattice dynamics.

Fig. 10(b) shows the pump–fluence dependence of the *amplitudes* A^{fs} and A^{ps} of the two relaxation components of $\Delta R/R$ measured at 1.55 eV, which were extracted with a bi–exponential fit as shown in Fig. 7(a). The inset of Fig. 10(b) also shows the intensity dependence of the sum of the two amplitudes A^{sum}=A^{fs}+A^{ps}, which follows an overall linear dependence on pump fluence that reflects the photocarrier density [56]. However, A^{sum} saturates at a high pump fluence ∼6 mJ/cm^2, while Fig 10(b) shows that the individual amplitudes A^{fs} and A^{ps} display different dependences on the pump fluence. This difference in the two components becomes more clear by plotting the ratio A^{fs}/A^{sum} at T=30K in Fig. 10(c). In particular, Fig. 10(c) demonstrates a *nonlinear threshold dependence* of the fs relaxation component. As seen by comparing Fig. 10(a) and Fig. 10(c), this threshold dependence of the low–temperature ratio A^{fs}/A^{sum} *coincides* with that of the pump–induced magneto–optical response ΔM measured at 200fs. At the same time, the relaxation times $\tau^{\rm fs}$ and $\tau^{\rm ps}$ remain fairly constant as function of pump fluence (see inset of Fig. 10(c)).

The above experimental results indicate a correlation between the emergence of fs AFM→FM switching at 200fs, above a pump fluence threshold that is not observed for ps time delays, with the threshold for nonlinear increase of the relative amplitude of the $\tau^{\rm fs}$ ∼500fs relaxation component. This result is consistent with our threoretical prediction that spin photoexcitation simultaneously leads to metallic behavior via a non–thermal electronic channel. Quasi–particle photoexcitation deforms the AFM background (FM correlation), which in turn increases the quasi–particle dispersion and softens the energy gap. This results in a quasi–instantaneous increase of the critical lattice displacement value $Q_c(t)$ below which the excitation gap closes. At the same time, the photoexcited carriers quasi–instantaneously change the effective lattice potential arising from electron–lattice coupling, which initiates lattice motion $Q(t)$ to a new equilibrium configuration $Q_{eq}(t) < Q$.

For low pump fluences, the photoinduced spin canting in the excited state is small, so there is no observable net magnetization and $Q(t) > Q_c$ similar to equilibrium. In this case, the photoinduced changes in the quasi–particle energy bands are small and mostly determined by the lattice motion $Q(t)$. The pump–fluence–dependence of the differential reflectivity is then approximately linear, determined by the non–thermal populations of "rigid" bands analogous to weakly correlated semiconductors [56]. Note, however, that the photexcitation will change the lattice spring constant as determined by the photocarrier population. With increasing pump fluence, a sufficiently large quasi–particle population of the metallic conduction band can result in significant quasi–instantaneous FM correlation between the AFM planes and chains, which in the presence of a symmetry–breaking magnetic field results in the observation of a net magnetization. As a result of laser–induced spin fluctuations, $\Delta J_z(t), \Delta\theta(t) > 0$ and the "soft" quasi–particle energy bands change, while the energy gap decreases. This results in the transient increase of the critical lattice displacement $Q_c(t)$ required for mainting an insulating state, so the lattice motion can easily close the gap.

A photoexcited magnetization is observed in our fs–resolved magneto–optical pump–probe signals during fs timescales above a critical pump fluence (Fig. 10(a)). Above this threshold, there are two possibilities: (i) $Q_c(t)$ exceeds the equilibrium lattice displacement Q. In this case, the fs photoexcitation "suddenly" quenches the insulator gap due to the photoinduced FM correlation within 100fs timescales. Such melting of the insulator gap can be induced instantaneously by composite fermion quasi–particle excitation as a result of nonadiabatic photoinduced $\Delta J_z(t) > 0$. Melting of the charge excitation gap can also be induced by an adiabatic spin canting angle $\Delta\theta(t) > 0$ (Fig. 6(b)). If $Q_c(t) > Q$, an insulator to metal transition can be "suddenly" induced without the need for lattice motion. (ii) $Q_c(t) < Q$ but $Q(t) \leq Q_c(t)$. In this case, lattice motion is required for the energy gap to close, so the insulator to metal transition is delayed as determined by the JT phonon period. In all cases, the lattice eventually reaches a transient state with smaller displacements $Q_{eq}(t)$ following population inversion between the polaronic valence band and metallic conduction band shown in Fig. 5.

The deviation of $Q_{eq}(t)$ from the equilibrium lattice configuration increases as the energy gap closes due to the differences between the e and h quasi–particles, whose photoexcitation results in a charge redistribution between bridge and corner sites. As discussed in the introduction, several ultrafast spectroscopy experiments indicate that quasi–thermal lattice evolution occurs during ps timescales, while non–thermal spin and charge populations are important during 100fs timescales. While the spin fluctuation and electronic hopping timescales are expected to be faster than the lattice oscillations, the exact time evolution leading to $Q(t) \leq Q_c(t)$ is beyond the scope of the present paper and may differ for individual materials. This lattice motion is not expected gto be a simple coherent phonon harmonic motion following strong photoexcitation of the metallic continuum of quasi–particle states $|E\rangle$.

CONCLUSIONS

To conclude, in this paper we described a possible mechanism for photoinduced insulator to metal and AFM to FM simultaneous transitions triggered by non–thermal population of a quasi–particle metallic conduction band induced by spin fluctuations and electron–magnon strong coupling. This mechanism involves a laser–induced nonlinear spin–charge–lattice coupling in the case of an AFM ground state consisting of FM chains and planes with JT distortions that stabilize the insulator energy gap. We propose that this mechanism may be relevant to explain the nonlinear pump fluence threshold dependencies of both magneto–optical (MOKE and MCD) and $\Delta R/R$ femtosecond signals measured in the PCMO manganite studied here. It may also be relevant to several other ultrafast spectroscopy experimental observations of nonlinear behavior during the non–thermal temporal regime following fs laser excitation of the AFM state of different insulating manganites [13, 14, 28–36]. In particular, we predict that electron–spin correlation leads to a broad conduction metallic band and quenches the electronic component of the insulator energy gap below a critical value of the JT lattice displacement that depends on the photoexcitation. Such laser–induced effects are pronounced in the case of composite fermion quasi–particles with "soft" energy bands, which mostly populate the lower magnetic Hubbard band due to the large Hund's rule interaction and excite spin fluctuations during electronic hopping timescales. FM correlation and spin canting during quasi–particle photoexcitation instantaneously increase the critical lattice displacement $Q_c(t)$ below which the energy gap closes, by changing the quasi–particle dispersions in a non–perturbative way. Above a critical photocarrier density, $Q_c(t)$ can become comparable to the equilibrium lattice distortion, which also decreases following lattice motion. Both effects act cooperatively to favor a non–equilibrium insulator to metal and AFM to FM simultaneous transitions. FM correlation induced by photoexcitation can trigger an instantaneous insulator to metal transition if $Q_c(t) \geq Q(t)$ during the laser pulse. The excitation of multiple quasi–particles should increase the above effect by enhancing the deformation of the AFM background. After the photoexcited quasi–electrons have relaxed on a fs timescale ($\tau^{\rm fs}$), electron–lattice and spin–lattice relaxation determines the subsequent ps dynamics ($\tau^{\rm ps}$).

The above theoretical framework, based on femtosecond magnetism induced by laser excitation, may be relevant for explaining several experimental observations when worked cooperatively with lattice deformation and free energy quasi–equilibrium effects. Based on the presently available experimental data and the uncertainties about the properties of the real materials, we cannot rule out other possible mechanisms for explaining the exprimentally observed fs spin and charge nonlinearities. Ultrafast coherent phonon dynamics, ultrafast lattice displacements that change the shape and distance of the individual chains and planes, structural phase transition, and melting of orbital order can all contribute to the observed effects and may work cooperatively with the proposed electronic/magnetic quasi–instantaneous mechanism and nonlinearities. For example, FM correlation arising from lattice distortions will change the quasi–particle energy dispersion, which depends on the changes in the hopping matrix elements for the local electronic configurations modified by electron–lattice strong local coupling. Such effects can be studied more directly with fs XRD, which unlike for conventional pump–probe spectroscopy can distinguish the different order parameter components. The observation of a time–dependent spring constant [28] and nonlinear dependence of the coherent phonon amplitudes on the pump intensity during non–thermal fs timescales are consistent with "soft" quasi–particle energy bands such as the ones proposed here. The lattice contribution is particularly important for the experimental observation of the ps τ^{ps} component, as Pr/Ca atoms will adapt to their final equilibrium positions at such ps time scales. Other interpretations may involve higher-order electronic scattering such as Auger Coulomb processes, which can increase the e–h quasi–particle populations via an avalanche effect during fs relaxation of the photocarriers. In all cases, any interpretations of the pump fluence nonlinear dependence must involve spin–flip dynamics in the excited state in order to explain the correlation to the "sudden" fs magnetization threshold behavior shown by both the MOKE and MCD magneto–optical signals. Our theory suggests a microscopic mechanism for such quasi–instantaneous spin–charge–lattice photoexcited effects, so we hope that it can open a discussion of whether the electronic/magnetic pathway proposed here creates a non–equilibrium initial condition that could initiate a photo—induced non–adiabatic phase transition. The "soft" energy bands of composite fermion quasi–particles make it easier to obtain a quasi–instantaneous insulator to metal and AFM to FM transitions as compared to bare electrons adiabatically decoupled from the spin background. In the latter case, due to the electronic order within a single zig–zag FM chain, the mechanism must rely on a more elaborate lattice motion [45] in order to close the energy gap. In addition, a complex energy landscape, possibly with multiple local min-

ima due to the elastic lattice potential $U_L(Q)$ [28, 54], should facilitate the phase transition mechanism proposed here, e.g. by creating metastable states. The insights from our theory–experiment results and our proposed "sudden quench" mechanism based on the "soft" quasi–particle energy bands may also prove useful for revealing the crucial many–body processes in other intertwined electronic phases, as the proximity of magnetic states appears ubiquitous with unconventional superconducting and exotic electronic phases in strongly correlated electronic materials [16]. In the long run, new insights can be gained by applying complementary ultrafast spectroscopy techniques, especially in the terahertz [57] and infrared spectral regions [58], and by combining spin and charge quantum fluctuations with quasi–equilibrium free energy and self–energy effects.

This work was supported by the Army Research Office under award W911NF-15-1-0135 (laser spectroscopy), and by the European Union's Seventh Framework Programme (FP7-REGPOT-2012-2013-1) under grant agreement No. 316165 (theory). The initial exploration was also supported in part by the National Science Foundation Contract No. DMR-1055352.

[1] D. S. Chemla, and J. Shah, Nature **411**, 549 (2001).
[2] V. M. Axt, and S. Mukamel, Rev. Mod. Phys. **70**, 145 (1998).
[3] M. E. Karadimitriou, E. G. Kavousanaki, K. M. Dani, N. A. Fromer, and I. E. Perakis, J. Phys. Chem. B **115**, 5634 (2011); M. E. Karadimitriou, E. G. Kavousanaki, I. E. Perakis, and K. M. Dani, Phys. Rev. B **82**, 165313 (2010).
[4] T. Li, A. Patz, L. Mouchliadis, J. Yan, T. A. Lograsso, I. E. Perakis, and J. Wang, Nature **496**, 69 (2013).
[5] T. Papenkort, T. Kuhn, and V. M. Axt, Phys. Rev. B 78, 132505 (2008); R. Matsunaga, Y. I. Hamada, K. Makise, Y. Uzawa, H. Terai, Z. Wang, and R. Shimano, Phys. Rev. Lett. 111, 057002 (2013).
[6] J. Bigot, M. Vomir, and E. Beaurepaire, Nature Physics **5**, 515 (2009).
[7] P. C. Lingos, J. Wang, and I. E. Perakis Phys. Rev. B 91, 195203 (2015); M. D. Kapetanakis, P. C. Lingos, C. Piermarocchi, J. Wang, and I. E. Perakis, Appl. Phys. Lett. **99**, 091111 (2011); M. D. Kapetanakis, I. E. Perakis, K. J. Wickey, C. Piermarocchi, and J. Wang, Phys. Rev. Lett. **103**, 047404 (2009).
[8] M. Porer, U. Leierseder, J.-M. Mnard, H. Dachraoui, L. Mouchliadis, I. E. Perakis, U. Heinzmann, J. Demsar, K. Rossnagel, and R. Huber, Nature Materials **13**, 857 (2014).
[9] E. Dagotto, T. Hotta, and A. Moreo, Phys. Rep. **344**, 1 (2001).
[10] Y.M. Sheu, S.A. Trugman, L. Yan, J. Qi, Q.X. Jia, A.J. Taylor, and R.P. Prasankumar, Phys. Rev. X **4**, 021001 (2014).
[11] H. Ichikawa, *et. al.*, Nature Mat., **10**, 2929 (2011).
[12] M.Fiebig, K. Miyano, Y Tomioka, and Y Tokura, Science **280**, 1925 (1998).
[13] D. Polli, M. Rini, S. Wall, R. W. Schoenlein, Y. Tomioka, Y. Tokura, G. Cerullo, and A. Cavalleri, Nature Mat. **6**, 643 (2007).
[14] M. Rini, R. Tobey, N. Dean, J. Itatani, Y. Tomioka, Y. Tokura, R. W. Schoenlein, and A. Cavalleri, Nature **449**, 72 (2007).
[15] G. C. Milward, M. J. Calderón, and P. B. Littlewood, Nature **433**, 607 (2005).
[16] A. Patz, T. Li, S. Ran, R. M. Fernandes, J. Schmalian, S. L. Budko, P. C. Canfield, I. E. Perakis, and J. Wang, Nat. Commun. **5**, 3229 (2014).
[17] S. G. Ovchinnikov and V. V. Valkov, *Hubbard Operators in the Theory of Strongly Correlated Electrons*, Imperial College Press (London, 2004).
[18] A. E. Ruckenstein and S. Schmitt-Rink, Phys. Rev. B **38**, 7188(R) (1988).
[19] V. M. Loktev and Yu. G. Pogorelov, Low Temp. Phys. **26**, 171 (2000).
[20] T. V. Ramakrishnan, H. R. Krishnamurthy, S. R. Hassan, and G. Venketeswara Pai, Phys. Rev. Lett. **92**, 157203 (2004); O. Cépas, H. R. Krishnamurthy, and T. V. Ramakrishnan, Phys. Rev. B **73**, 035218 (2006).
[21] T. V. Ramakrishnan, J. Phys. Condens. Matter **19**, 125211 (2007).
[22] D. Basov, R. D. Averitt, M. Dressel, D. Vandermarel, and K. Haule, Rev. Mod. Phys. **83**, 471 (2011).
[23] A. J. Millis, P. B. Littlewood, and B. I Shraiman, Phys. Rev. Lett. **74**, 5144 (1995).
[24] K. I. Kugel, A. L. Rakhmanov, and A. O. Sboychakov, Phys. Rev. Lett. **95**, 267210 (2005); A. O. Sboychakov, K. I. Kugel, and A. L. Rakhmanov, Phys. Rev. B **74**, 014401 (2006).
[25] D. Wegkamp and J. Stahler, Progress in Surface Science **90**, 464 (2015).
[26] A. Subedi, A. Cavalleri, and A. Georges, Phys. Rev. B **89**, 220301(R) (2014).
[27] V. R. Morrison, R. P. Chatelain, K. L. Tiwari, A. Hendaoui, A. Bruhacs, M. Chaker, and B. Siwick, Science 346, 445 (2014).
[28] P. Beaud, A. Caviezel, S. O Mariager, L. Rettig, G. Ingold, C. Dornes, S.-W. Huang, J. A. Johnson, M. Radovic, T. Huber, T. Kubacka, A. Ferrer, H. T. Lemke, M. Chollet, D. Zhu, J. M. Glownia, M. Sikorski, A. Robert, H. Wadati, M. Nakamura, M. Kawasaki, Y. Tokura, S. L. Johnson, and U. Staub, Nature Materials **13**, 923 (2014).
[29] M. Först, R. I. Tobey, S. Wall, H. Bromberger, V. Khanna, A. L. Cavalieri, Y.-D. Chuang, W. S. Lee, R. Moore, W. F. Schlotter, J. J. Turner, O. Krupin, M. Trigo, H. Zheng, J. F. Mitchell, S. S. Dhesi, J. P. Hill, and A. Cavalleri, Phys. Rev. B **84**, 241104(R) (2011).
[30] K. Miyasaka, M. Nakamura, Y. Ogimoto, H. Tamaru, and K. Miyano, Phys. Rev. B **74**, 012401 (2006).
[31] M. Matsubara, Y. Okimoto, T. Ogasawara, Y.Tomioka, H. Okamoto, and Y. Tokura, Phys. Rev. Lett. **99**, 207401 (2007).
[32] Y. Okimoto, H. Matsuzaki, Y. Tomioka, I. Kezsmarki, T. Ogasawara, M. Matsubara, H. Okamoto, and Y. Tokura, J. Phys. Soc. Jpn. **76**, 043702 (2007).
[33] S. Wall, D. Prabhakaran, A. T. Boothroyd, and A. Cavalleri, Phys. Rev. Lett. **103**, 097402 (2009).
[34] H. Ehrke, R. I. Tobey, S. Wall, S. A. Cavill, M. Först, V. Khanna, Th. Garl, N. Stojanovic, D. Prabhakaran, A. T. Boothroyd, M. Gensch, A. Mirone, P. Reutler, A. Revcolevschi, S. S. Dhesi, and A. Cavalleri, Phys. Rev. Lett. **106**, 217401 (2011).
[35] H. Matsuzaki, H. Uemura, M. Matsubara, T. Kimura, Y. Tokura, and H. Okamoto, Phys. Rev. B **79**, 235131 (2009).
[36] R. Singla, A. Simoncig, M. Först, D. Prabhakaran, A. L. Cavalieri, and A. Cavalleri, Phys. Rev. B 88, 075107 (2013).
[37] P. W. Anderson and H. Hasegawa, Phys. Rev. **100**, 675 (1955); P.–G. de Gennes, Phys. Rev. **118**, 141 (1960).
[38] J.P.F. LeBlanc, A. E. Antipov, F. Becca, I. W. Bulik, GarnetKin-Lic Chan , C.-M. Chung, Y. Deng, M. Ferrero, T. M. Henderson, C. A. Jiménez-Hoyos, E. Kozik, X.-W. Liu, A. J. Millis,

N.V. Prokofév, Mingpu Qin, G. E. Scuseria, H. Shi, B.V. Svistunov, L. F. Tocchio, I.S. Tupitsyn, S. R. White, S. Zhang, B.-X. Zheng, Z. Zhu, and E. Gull Phys. Rev. X **5**, 041041 (2015).
[39] M. D. Kapetanakis and I. E. Perakis, Phys. Rev. Lett. **101**, 097201 (2008); Phys. Rev. B **78**, 155110 (2008).
[40] M. D. Kapetanakis and I. E. Perakis, Phys. Rev. B **75**, 140401(R) (2007); M. D. Kapetanakis, A. Manousaki, and I. E. Perakis Phys. Rev. B 73, 174424 (2006).
[41] F. Ye, P. Dai, J. A. Fernandez-Baca, H. Sha, J. W. Lynn, H. Kawano-Furukawa, Y. Tomioka, Y. Tokura, and J. Zhang, Phys. Rev. Lett. 96, 047204 (2006); F. Ye, P. Dai, J. A. Fernandez-Baca, D. T. Adroja, T. G. Perring, Y. Tomioka, and Y. Tokura, Phys. Rev. B 75, 144408 (2007).
[42] J. C. Hubbard, Proc. Roy. Soc. A **276**, 238 (1963); *ibid* **281**, 401 (1964); *ibid* **285**, 542 (1965).
[43] F. C. Zhang and T. M. Rice, Phys. Rev B **37**, 3759 (1988)
[44] V. Ferrari, M. Towler, and P. B. Littlewood, Phys. Rev. Lett. **91**, 227202 (2003)
[45] M. van Veenendaal, Phys. Rev. B **94**, 115101 (2016).
[46] A. Tanaka, J. Phys. Soc. Japan **72**, 2433 (2003); ibid **73**, 152 (2004).
[47] P. G. Radaelli, D. E. Cox, M. Marezio, and S.–W. Cheong, Phys. Rev. B **55**, 3015 (1997).
[48] A. Daoud-Aladine, J. Rodrìguez-Carvajal, L. Pinsard-Gaudart, M. T. Fernández-Díaz, and A. Revcolevschi, Phys. Rev. Lett. **89**, 097205 (2002); D. J. García, K. Hallberg, C. D. Batista, M. Avignon, and B. Alascio, Phys. Rev. Lett. **85**, 3720 (2000); C. I. Ventura and B. Alascio, Phys. Rev. B **68**, 020404(R) (2003).
[49] G. Knizia and GarnetKin-Lic Chan, Phys. Rev. Lett. **109**, 186404 (2012).
[50] Z. He and A. J. Millis, Phys. Rev. B **93**, 115126 (2016).
[51] M. van Veenendaal, Phys. Rev. B **87**, 235118 (2013).
[52] J. Herrero–Martin, J. Blasco, J. Garcia, G. Subias, and C. Mazzoli, Phys. Rev. B **83**, 184101 (2011).
[53] J. van den Brink, G. Khaliullin, and D. Khomskii, Phys. Rev. Lett. **83**, 5118 (1999).
[54] K. H. Ahn, T. Lookman, and A. R. Bishop, Nature **428**, 401 (2004); K. H. Ahn, T. F. Seman, T. Lookman, and A. R. Bishop, Phys. Rev. B **88**, 144415 (2013).
[55] T. N. Todorov, J. Phys. Condens. Matter. **13**, 10125 (2001).
[56] H. J. Zeiger, J. Vidal, T. K. Cheng, E. P. Ippen, G. Dresselhaus, and M. S. Dresselhaus, Phys. Rev. B **45**, 768 (1992).
[57] L. Luo, I. Chatzakis, A. Patz, and J. Wang, Phys. Rev. Lett. **114**, 107402 (2015); L. Luo, I. Chatzakis, J. Wang, F. B. P. Niesler, M. Wegener, T. Koschny, and C. M. Soukoulis, Nat. Commun. **5**, 3055 (2014); I. Chatzakis, L. Luo, J. Wang, N.-H. Shen, T. Koschny, J. Zhou, and C. M. Soukoulis, Phys. Rev. B **86**, 125110 (2012).
[58] J. Wang, M. W. Graham, Y. Ma, G. R. Fleming, and R. A. Kaindl, Phys. Rev. Lett. **104**, 177401 (2010); T. Li, L. Luo, M. Hupalo, J. Zhang, M. C. Tringides, J. Schmalian, and J. Wang, Phys. Rev. Lett. **108**, 167401 (2012); J. Wang, G. A. Khodaparast, J. Kono, A. Oiwa, and H. Munekata, J. of Mod. Opt. **51**, 2771 (2004); J Wang, GA Khodaparast, J Kono, T Slupinski, A Oiwa, H Munekata, Journal of superconductivity, **16**, 373 (2003)

APPENDIX

The quantum kinetic equations of motion for the spin–dependent local populations are obtained by using the Hamiltonian Eq.(6) as follows:

$$\partial_t \rho_i^{\alpha}(M) = 2\, Im \sum_{\sigma'=\pm 1} F_{\sigma'}(M) \times$$
$$\sum_{l\alpha'} V_{\alpha'\alpha}(l-i)\langle \left[\cos\left(\frac{\theta_l-\theta_i}{2}\right) \hat{e}^{\dagger}_{\alpha'\sigma'}(l) - \sigma' \sin\left(\frac{\theta_l-\theta_i}{2}\right) \hat{e}^{\dagger}_{\alpha'-\sigma'}(l) \right] \hat{e}_{\alpha\sigma'}(iM)\rangle, \tag{34}$$

$$\partial_t \rho_i(m) = -2Im \sum_{\alpha} \sum_{\sigma'} F_{\sigma'}(m+\frac{\sigma'}{2}) \times$$
$$\sum_{l\alpha'} V_{\alpha'\alpha}(l-i)\langle \left[\cos\left(\frac{\theta_l-\theta_i}{2}\right) \hat{e}^{\dagger}_{\alpha'\sigma'}(l) - \sigma' \sin\left(\frac{\theta_l-\theta_i}{2}\right) \hat{e}^{\dagger}_{\alpha'-\sigma'}(l) \right] \hat{e}_{\alpha\sigma'}(i, m+\frac{\sigma'}{2})\rangle. \tag{35}$$

The above equations are exact in the limit $J_H \to \infty$ and describe the dynamical coupling of site i to the rest of the lattice, driven by the charge flucuations described by $H_{hop}(t)$, Eq.(8). This inter–site coupling is determined by the (exact) equation of motion

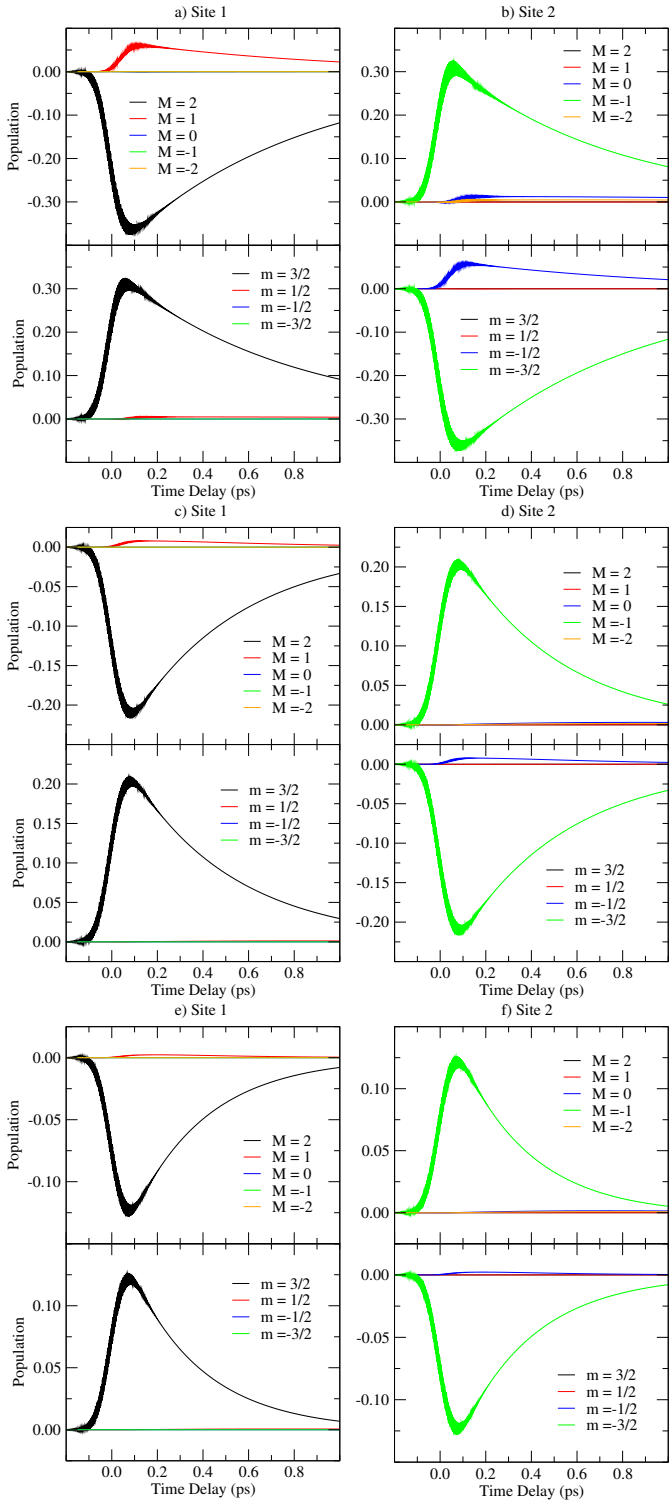

FIG. 2. (Color online) Time–dependent changes in the populations of the local configurations $|i\alpha M\rangle$ (upper panels) and $|im\rangle$ (lower panels) of the two AFM sites i=1,2 discussed in the text for population lifetime T_1=1ps and different dephasing times T_2: (a)–(b): T_2=50fs, (c)–(d): T_2=15fs, (e)–(f): T_2=8fs. The spin quantization axis was taken parallel to the equilibrium spin direction in site 1.

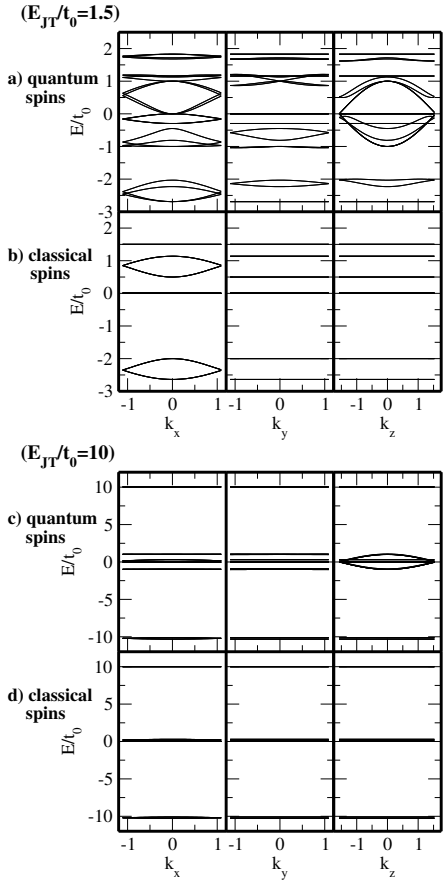

FIG. 3. Calculated energy dispersions of composite–fermion quasi–particles and comparison to bare electrons for intermediate ((a) and (b)) and large ((c) and (d)) values of JT energy barrier E_{JT}. (a), (c): Quantum spins (S=3/2), (b), (d): Classical spins ($S \to \infty$).

$$
\begin{aligned}
& i\partial_t \langle \hat{e}^\dagger_{\beta\bar{\sigma}}(j)\, \hat{e}_{\alpha\sigma}(iM)\rangle - [\varepsilon_{\alpha\sigma}(i) - \varepsilon_{\beta\bar{\sigma}}(j)]\ \langle \hat{e}^\dagger_{\beta\bar{\sigma}}(j)\, \hat{e}_{\alpha\sigma}(iM)\rangle \\
& = \sum_{l\sigma'} \sum_{\alpha'\beta'} V_{\alpha'\beta'}(l-j)\ \cos\left(\frac{\theta_l - \theta_j}{2}\right)\ \langle [\hat{e}^\dagger_{\beta\bar{\sigma}}(j), \hat{e}_{\beta'\sigma'}(j)]_+\, \hat{e}^\dagger_{\alpha'\sigma'}(l)\, \hat{e}_{\alpha\sigma}(iM)\rangle \\
& - \sum_{l\sigma'} \sum_{\alpha'\beta'} V_{\alpha'\beta'}(i-l)\ \cos\left(\frac{\theta_l - \theta_i}{2}\right)\ \langle \hat{e}^\dagger_{\beta\bar{\sigma}}(j)\, \hat{e}_{\beta'\sigma'}(l)\, [\hat{e}^\dagger_{\alpha'\sigma'}(i), \hat{e}_{\alpha\sigma}(iM)]_+ \rangle \\
& + \sum_{l\sigma'} \sum_{\alpha'\beta'} V_{\alpha'\beta'}(l-j)\, \sigma'\ \sin\left(\frac{\theta_l - \theta_j}{2}\right)\ \langle [\hat{e}^\dagger_{\beta\bar{\sigma}}(j), \hat{e}_{\beta'-\sigma'}(j)]_+\, \hat{e}^\dagger_{\alpha'\sigma'}(l)\, \hat{e}_{\alpha\sigma}(iM)\rangle \\
& + \sum_{l\sigma'} \sum_{\alpha'\beta'} V_{\alpha'\beta'}(i-l)\, \sigma'\ \sin\left(\frac{\theta_l - \theta_i}{2}\right)\ \langle \hat{e}^\dagger_{\beta\bar{\sigma}}(j)\, \hat{e}_{\beta'-\sigma'}(l)\, [\hat{e}^\dagger_{\alpha'\sigma'}(i), \hat{e}_{\alpha\sigma}(iM)]_+ \rangle, \qquad (36)
\end{aligned}
$$

which involves four–particle density matrices of Hubbard operators. The differences from the familiar equations of motion for e–h coherence of bare electrons in weakly–correlated systems [1, 2] arise from the composite fermion anti–commutators $[\hat{e}^\dagger_{\alpha'\sigma'}(i), \hat{e}_{\alpha\sigma}(iM)]_+$, Eq.(2). The latter deviate from fermion behavior due to the suppressed population of the higher magnetic Hubbard band states with total spin J=$S-1/2$, which leads to the coupling of higher density matrices and a many–body hierarchy if the bosonic on–site fluctuations in Eq.(2) are strong.

In the deep insulating limit, spin exchange is primarily determined by charge fluctuations between neighboring atoms

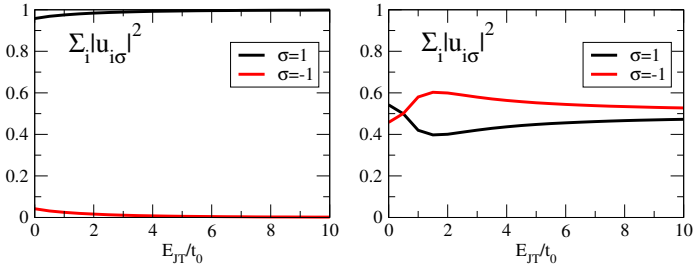

FIG. 4. (Color online) Calculated probability of flipped spins for quasi–particles below (left panel) and above (right panel) the energy gap. σ=1 (-1) means quasi–particle total spin parallel (anti–parallel) to the equilibrium spin direction determined by θ_i=0 or π. The pronounced difference in quantum spin canting between a quasi–electron and a quasi–hole correlates with the difference in their energy dispersions shown in Fig. 3.

[20, 21]. Separating such short–range inter–site correlation in Eq.(36) we obtain

$$
\begin{aligned}
& i\partial_t \langle \hat{e}^\dagger_{\beta\bar{\sigma}}(j)\,\hat{e}_{\alpha\sigma}(iM)\rangle - [\varepsilon_{\alpha\sigma}(i)-\varepsilon_{\beta\bar{\sigma}}(j)]\ \langle \hat{e}^\dagger_{\beta\bar{\sigma}}(j)\,\hat{e}_{\alpha\sigma}(iM)\rangle \\
& = \sum_{\sigma'}\sum_{\alpha'\beta'} V_{\alpha'\beta'}(i-j)\ \cos\left(\frac{\theta_i-\theta_j}{2}\right)\ \Big[\langle \hat{e}_{\beta'\sigma'}(j)\hat{e}^\dagger_{\beta\bar{\sigma}}(j)\,\hat{e}^\dagger_{\alpha'\sigma'}(i)\,\hat{e}_{\alpha\sigma}(iM)\rangle - \langle \hat{e}^\dagger_{\beta\bar{\sigma}}(j)\,\hat{e}_{\beta'\sigma'}(j)\,\hat{e}_{\alpha\sigma}(iM)\,\hat{e}^\dagger_{\alpha'\sigma'}(i)\rangle\Big] \\
& + \sum_{\sigma'}\sum_{\alpha'\beta'} V_{\alpha'\beta'}(i-j)\,\sigma'\ \sin\left(\frac{\theta_i-\theta_j}{2}\right)\ \Big[\langle \hat{e}_{\beta'-\sigma'}(j)\hat{e}^\dagger_{\beta\bar{\sigma}}(j)\,\hat{e}^\dagger_{\alpha'\sigma'}(i)\,\hat{e}_{\alpha\sigma}(iM)\rangle - \langle \hat{e}^\dagger_{\beta\bar{\sigma}}(j)\,\hat{e}_{\beta'-\sigma'}(j)\,\hat{e}_{\alpha\sigma}(iM)\hat{e}^\dagger_{\alpha'\sigma'}(i)\rangle\Big] \\
& + \sum_{l\neq i,j}\sum_{\sigma'}\sum_{\alpha'\beta'} V_{\alpha'\beta'}(l-j)\ \cos\left(\frac{\theta_l-\theta_j}{2}\right)\ \langle [\hat{e}^\dagger_{\beta\bar{\sigma}}(j),\hat{e}_{\beta'\sigma'}(j)]_+\,\hat{e}^\dagger_{\alpha'\sigma'}(l)\,\hat{e}_{\alpha\sigma}(iM)\rangle \\
& - \sum_{l\neq i,j}\sum_{\sigma'}\sum_{\alpha'\beta'} V_{\alpha'\beta'}(i-l)\ \cos\left(\frac{\theta_l-\theta_i}{2}\right)\ \langle \hat{e}^\dagger_{\beta\bar{\sigma}}(j)\,\hat{e}_{\beta'\sigma'}(l)\,[\hat{e}^\dagger_{\alpha'\sigma'}(i),\hat{e}_{\alpha\sigma}(iM)]_+\,\rangle \\
& + \sum_{l\neq i,j}\sum_{\sigma'}\sum_{\alpha'\beta'} V_{\alpha'\beta'}(l-j)\,\sigma'\ \sin\left(\frac{\theta_l-\theta_j}{2}\right)\ \langle [\hat{e}^\dagger_{\beta\bar{\sigma}}(j),\hat{e}_{\beta'-\sigma'}(j)]_+\,\hat{e}^\dagger_{\alpha'\sigma'}(l)\,\hat{e}_{\alpha\sigma}(iM)\rangle \\
& + \sum_{l\neq i,j}\sum_{\sigma'}\sum_{\alpha'\beta'} V_{\alpha'\beta'}(i-l)\,\sigma'\ \sin\left(\frac{\theta_l-\theta_i}{2}\right)\ \langle \hat{e}^\dagger_{\beta\bar{\sigma}}(j)\,\hat{e}_{\beta'-\sigma'}(l)\,[\hat{e}^\dagger_{\alpha'\sigma'}(i),\hat{e}_{\alpha\sigma}(iM)]_+\rangle. \qquad (37)
\end{aligned}
$$

where the last four terms describe the coupling of the quantum dimer consisting of neigboring sites (i,j) with the rest of the lattice. The time–dependent local spin dynamics discussed in Section III was obtained by factorizing the product of on–site operators (local populations) between sites i and j on the rhs of the above equation and neglecting the long–range coherence arising from their coupling to the environment sites $l \neq (i,j)$. We thus obtain the following equation of motion that describes the charge–spin fluctuations between neigboring sites:

$$
\begin{aligned}
& i\partial_t \langle \hat{e}^\dagger_{\beta\bar{\sigma}}(j)\,\hat{e}_{\alpha\sigma}(iM)\rangle - [\varepsilon_{\alpha\sigma}(i)-\varepsilon_{\beta\bar{\sigma}}(j)]\ \langle \hat{e}^\dagger_{\beta\bar{\sigma}}(j)\,\hat{e}_{\alpha\sigma}(iM)\rangle = V_{\alpha\beta}(i-j)\,F_\sigma(M)\times \\
& \left[\delta_{\sigma,\bar{\sigma}}\cos\left(\frac{\theta_i-\theta_j}{2}\right)+\sigma\delta_{\sigma,-\bar{\sigma}}\ \sin\left(\frac{\theta_i-\theta_j}{2}\right)\right]\sum_{M'} F^2_{\bar{\sigma}}(M')\left[\rho^\alpha_i(M)\,\rho_j(M'-\frac{\bar{\sigma}}{2})-\rho_i(M-\frac{\sigma}{2})\,\rho^\beta_j(M')\right]. \qquad (38)
\end{aligned}
$$

Eqs.(34), (35), and (38) provide a closed system of equations of motion. They define quantum master equations for describing the local spin dynamics in a real–space picture that treats both on–site and nearest–neigbor spin and charge correlations.

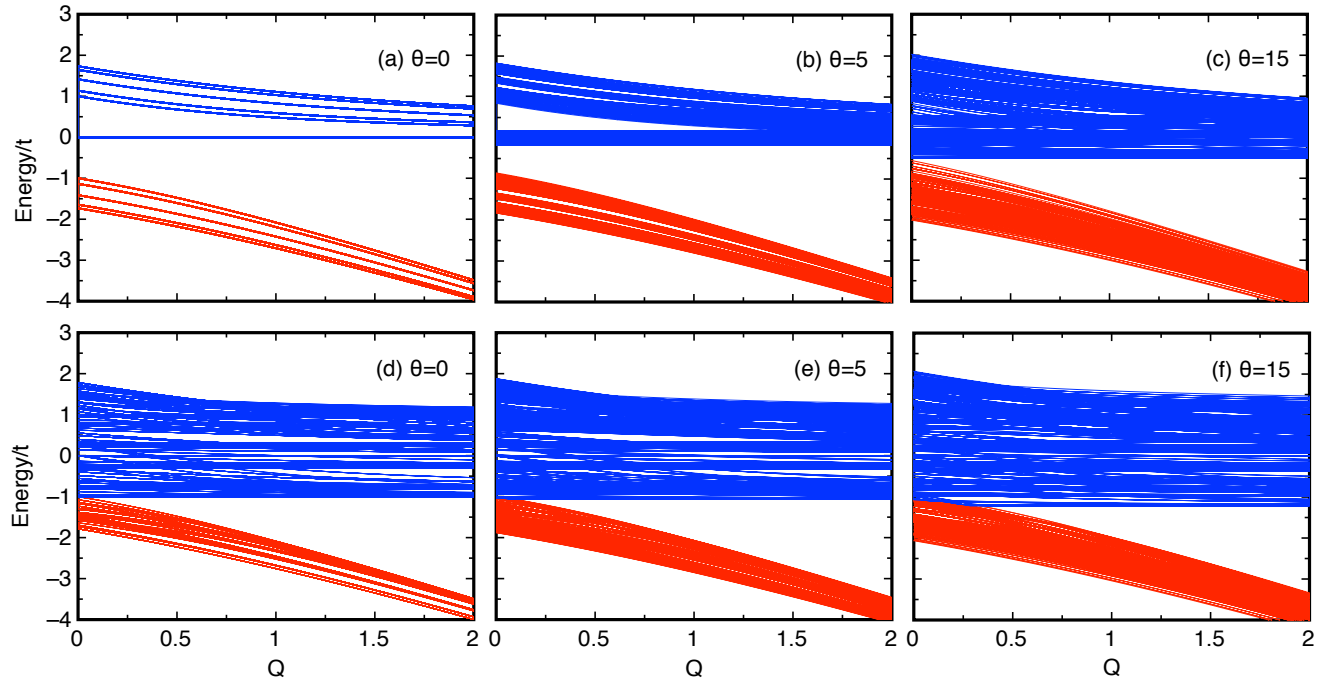

FIG. 5. (Color online) Calculated energy levels as function of lattice displacement, E_{JT}=$\varepsilon_{JT}Q$, for different spin canting angles θ. The latter describes FM correlation between the FM chains and planes with respect to the collinear AFM state θ=0. Upper panel: Bare electrons (adiabatically–decoupled classical spins, $S \rightarrow \infty$). Lower panel: Composite fermion quasi–particles (strongly–coupled quantum spins, S=3/2). $\varepsilon_{JT} = 1.6t_0$.

Such an approximation gives the results of Fig. 1(c) and Fig. 2, while recovering the effective inter–site FM exchange interaction of Refs. [20, 21]. Unlike for the standard double exchange model [37], the latter FM interaction is obtained in the insulating limit with JT lattice distortions. Here such short–range FM correlation is modified away from equilibrium by the coupling of a strong laser field, which controls the charge transfer across the JT energy barrier. The product of local populations that enters on the rhs of Eq.(38) depends on the laser excitation and describes a population–inversion nonlinearity and nonlinear saturation, whose effect on the spin dynamics and short–range FM correlation is seen in Fig. 1(c).

In the opposite limit of itinerant quasi–particles, we truncate the hierarchy of equations of motion by factorizing the four–particle density matrices of *composite fermions* that enter in Eq.(36):

$$\langle [\hat{e}^{\dagger}_{\beta\bar{\sigma}}(j), \hat{e}_{\beta'\sigma'}(j)]_+ \, \hat{e}^{\dagger}_{\alpha'\sigma'}(l)\, \hat{e}_{\alpha\sigma}(iM)\rangle = \langle [\hat{e}^{\dagger}_{\beta\bar{\sigma}}(j), \hat{e}_{\beta'\sigma'}(j)]_+ \rangle \langle \hat{e}^{\dagger}_{\alpha'\sigma'}(l)\, \hat{e}_{\alpha\sigma}(iM)\rangle, \tag{39}$$

where $j \neq l, i$. The above mean field approximation neglects fluctuations in the composite fermion anticommutator $[\hat{e}^{\dagger}_{\beta\sigma}(j), \hat{e}_{\beta'\sigma'}(j)]_+$ as in the Hubbard–I approximation [17, 42] and results in Eq.(18). The difference from bare electrons is described by the deviations of the composite fermion quasi–particle anticommutators $n_{\alpha\sigma}(i)$, Eq.(19), from their fermionic values, which is due to the suppression of the populations of the J=$S - 1/2$ total spin configurations during the electronic motion by the strong Hund's rule exchange interaction J_H.

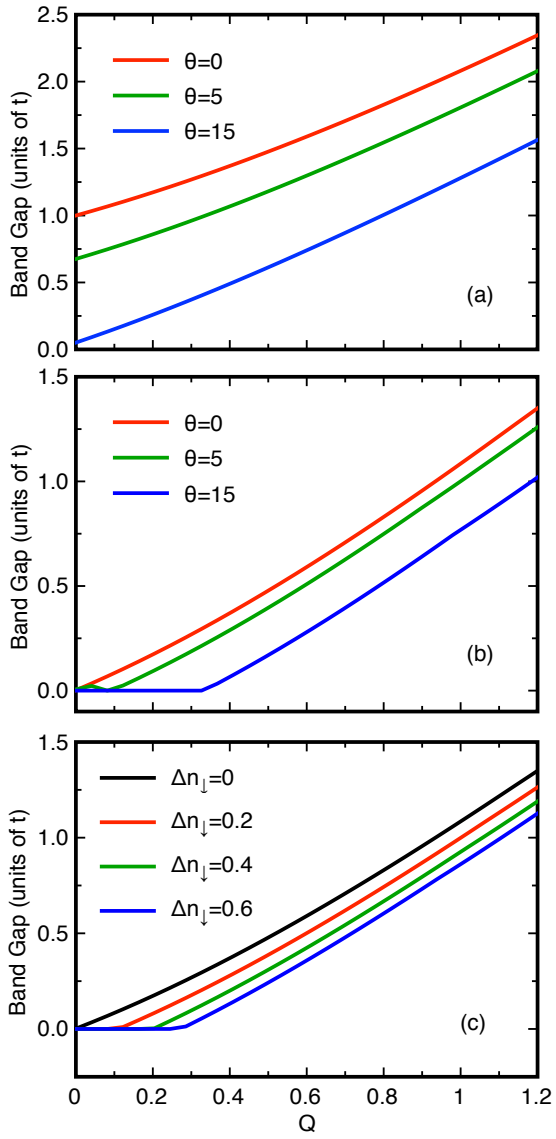

FIG. 6. (Color online) Effect of FM correlation on the lattice dependence of the energy gap of Fig. 5. (a) bare electrons, increasing θ, (b) composite fermion quasi–particles, increasing θ, (c) composite fermion quasiparticles, increasing ΔJ_z.

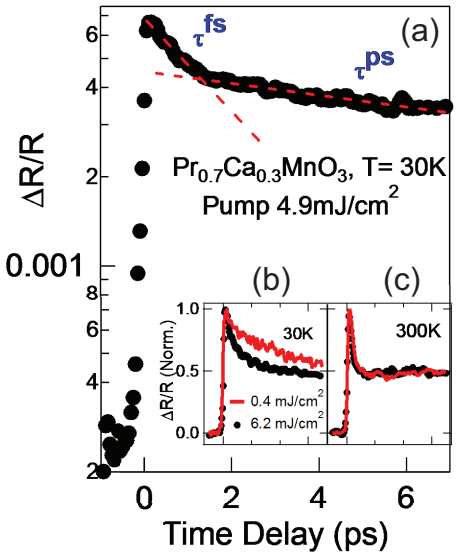

FIG. 7. (Color online) (a) Femtosecond–resolved ΔR/R for 1.55eV pump/probe excitation, plotted on a log–scale. Dashed lines highlight two distinct components of bi–exponential decay. (b)-(c): Comparison of normalized ΔR/R for high and low pump fluences at temperatures (b) 30K (below the AFM transition) and (c) 300K (above the CO/OO and AFM transitions)

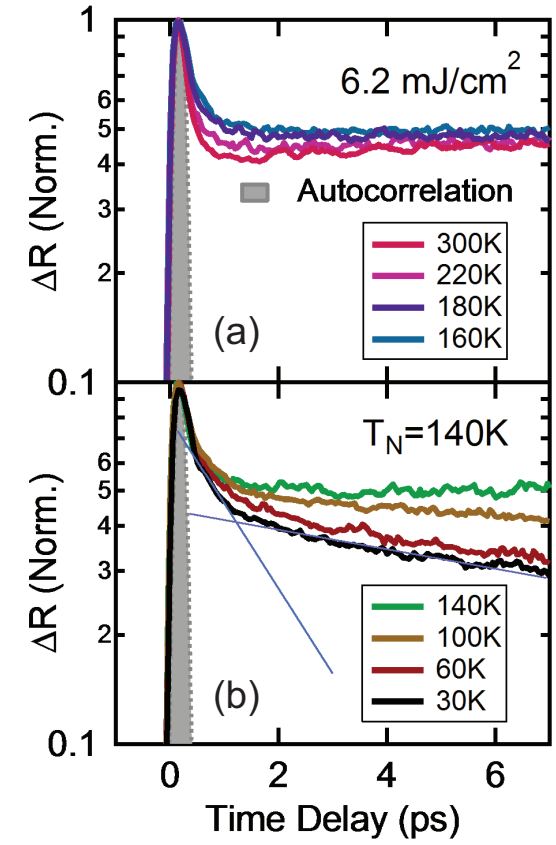

FIG. 8. (Color online) Detailed temperature dependence of the fs–resolved ΔR/R, shown on a log–scale together with the pulse autocorrelation (shade) for (a) 300K, 220K, 180K and 160K above the AFM transition temperature ; (b) 140K, 100K, 60K and 30K below the AFM transition temperature. The distinct $\tau^{\rm fs}$ and $\tau^{\rm ps}$ relaxation components are marked for the 30K trace (blue lines).

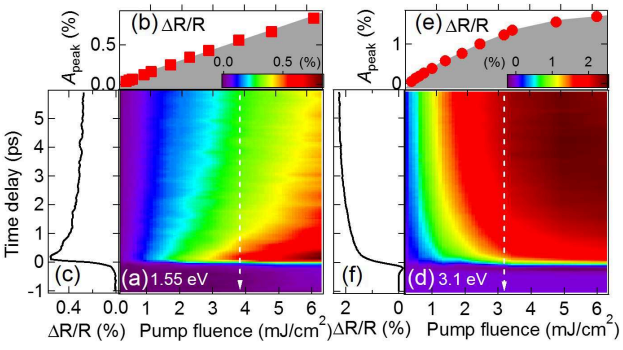

FIG. 9. (Color online) (a)-(c): Ultrafast ΔR/R dynamics for degenerate 1.55eV pump/probe photoexcitation. (a): 2D dependence on pump fluence and time delay at 30K; (b): peak amplitude as function of pump fluence; (c): temporal trace at pump fluence of 3.8mJ/cm^2 marked in (a). (d)–(f): Same ΔR/R plot as above, but for non–degenerate photoexcitation with 1.55eV pump but 3.1eV probe.

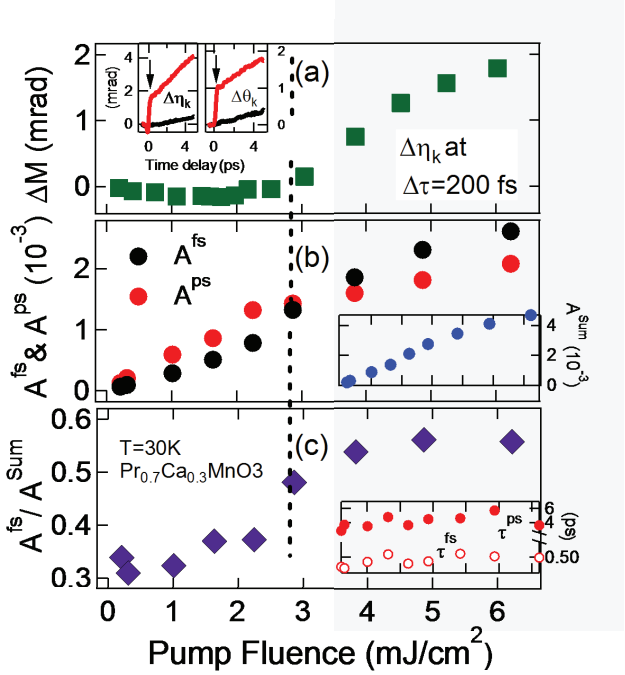

FIG. 10. (Color online) Dependence of spin and charge dynamics on photoexcitation intensity. (a): Photoinduced fs magnetization ΔM extracted from magneto–optical ellipticity signal $\Delta\eta_k$ at 200fs (green rectangle). Inset: Comparison of $\Delta\eta_k$ and $\Delta\theta_k$ (Kerr rotation) dynamics for 5.6mJ/cm^2 (red) and 0.8mJ/cm^2 (black). Both signals show the same "sudden" fs jump above an intensity threshold, which we thus attribute to photoinduced magnetization during 100fs timescales (arrow). All error bars are within the markers. (b): Amplitudes of fast component A_{fs} (black dots), slow component A_{ps} (red dots), and A^{sum}= A_{fs}+ A_{ps} (inset) of our bi–exponential fit of $\Delta R(t)/R$. (c): Fraction F=A^{fs}/A^{sum} (blue rhombus) and the two distinct relaxation times (inset) as function of pump intensity.